ESWL-DERIVED PARTICLE SIZE DISTRIBUTIONS AND FRACTURE GEOMETRIES: A CONTEXTUAL GEOBIOMED FRAMEWORK FOR ASSESSMENT OF KIDNEY STONE RECURRENCE

BY

LAUREN G. TODOROV

THESIS

Submitted in partial fulfillment of the requirements
for the degree of Master of Science in Geology
with a minor in College Teaching
in the Graduate College of the
University of Illinois Urbana-Champaign, 2022

Urbana, Illinois

Adviser:

Professor Bruce William Fouke

ABSTRACT

Extracorporeal shock wave lithotripsy (ESWL) is a common worldwide clinical treatment for human kidney stones. Yet its 60% success rate is counterbalanced by recurrence rates of 50% within 10 years with no effective treatments currently available. This study has applied GeoBioMed approaches to determine the fracture patterns and grain size distributions of ESWL-derived particles within the context of their original crystalline architecture as revealed by high- and super-resolution autofluorescence (SRAF) microscopy. Calcium oxalate (CaOx) stones were removed from a Mayo Clinic patient using standard percutaneous nephrolithotomy (PCNL) and shock pulse lithotripsy (SPL). This produced ~4-12mm-diameter PCNL-derived fragments that were treated *ex vivo* to form 100s of smaller ESWL-derived particles. ESWL-induced fractures propagated in a variety of geometric orientations relative to the original crystalline architecture of each fragment to form rectangular, pointed, concentrically spalled, and irregular ESWL-derived particles size frequency distributions ranged from very fine silt (4-8μm) to very fine pebbles (2-4mm), with a mean of fine sand (125-250μm). These particles are smaller than the 3-4mm-diameter detection limit of clinical microcomputed tomography (micro-CT) and are hydrodynamically retained on internal kidney membrane surfaces. ESWL therefore produces small undetectable crystallization seed points distributed throughout the kidney that dramatically increase geochemical reactive surface area and kinetically enhance stone recurrence.

ACKNOWLEDGMENTS

I would like to acknowledge and give my warmest thanks to my supervisor, Dr. Bruce W. Fouke, who made this interdisciplinary work possible. His guidance, advice, and persistent help carried me through all stages of my current and past projects on the mechanisms of universal biomineralization in corals, stromatolites, subsurface microbial environments, and kidney stones. His continuous spirit of adventure regarding research, service, outreach, and teaching inspires me every day. I am so honored to have been able to work with my role model and hope that I can one day be the same for my future students. I would also like to thank my co-advisor, Dr. Mayandi Sivaguru, for his hands-on microscopy training, as well as brilliant comments and suggestions. With both of their guidance and support, I have undoubtingly become a better scientist, science communicator, and mentor. I am grateful to have had the opportunity to train in such an intellectually stimulating and supportive environment.

This research is dedicated to my dear family, who came to the United States from Bulgaria to provide me with a world of opportunity.

I would like to thank my father, who was a constant source of support, guidance, and inspiration, and my mother, who encouraged me to be my most creative and authentic self. Although my mother is no longer of this world, I will carry her legacy of love and teaching with me throughout my personal and professional career. I would also like to share my gratitude towards my sister for her help and guidance during my academic progress, especially in my younger years.

My family has given me the drive and discipline to tackle any task with enthusiasm and determination. Without their love, support, and sacrifices, this project would not have been made possible.

TABLE OF CONTENTS

CHAPTER 1
INTRODUCTION

The prevalence and incidence of patients with kidney stones worldwide has increased dramatically over the last four decades, with these trends exhibiting substantial geographic variability (Thongprayoon et al., 2020). This is globally observed in all cohorts of sex, age, ethnicity, and race, which exhibit substantial geographic variability ranging from 3-15% in the United States, 1-19% in Asia, 4% in South America, 5-10% in Europe, and 20-25% in the Middle East (Trinchieri et al., 2000; Stamatelou et al., 2003; Hesse et al., 2003; Penniston et al., 2011; Scales et al., 2012; Najeeb et al., 2013; Villarroel and Blackwell, 2019; Khan et al., 2016; Pfau and Knauf, 2016; Zisman, 2017; Liu et al., 2018; *Urological Diseases in America, 2012;* Thongprayoon et al., 2020, Abufaraj et al., 2021). However, some significant proportion of these increases likely result from improved medical imaging (primarily microcomputed tomography; micro-CT), as well as uncertainty resulting from inconsistencies in diagnostic codes and self-reporting, stone terminology and classification, risk factor identification, and uncertainties in the prediction and monitoring of stone recurrence (Thongprayoon et al., 2020). A definitive diagnosis of symptomatic kidney stones therefore still fundamentally depends upon an actual stone being imaged, observed when surgically removed, or after being voided (Thongprayoon et al., 2020).

As a result of these complex intertwined factors, extracorporeal shock wave lithotripsy (ESWL), remains the most common non-invasive *in vivo* clinical intervention because it is relatively low-cost and approximately 60% effective in fragmenting and eliminating kidney stones less than ~11mm in diameter (Köhrmann et al., 1993; Miller and Lingeman, 2007; Keeley et al., 1999; Khan et al., 2016; Brain et al., 2021). Current clinical approaches consider ESWL-derived residual stone particles that are <3-4mm in diameter to be “clinically insignificant residual

fragments" because they are assumed to be spontaneously passed, causing patients to be classified as being in a "stone free state" and thus not requiring further treatment (Sabnis et al., 1997; Keeley et al., 1999; Osman et al., 2005; Kang et al., 2016). However, ESWL patients also experience staggering stone recurrence rates of as much as 50% within 10 years, which may result from crystallization at sites of ESWL-induced tissue damage as observed in renal histology sections (McAteer and Evan, 2008; Evan et al., 2015). Recurrence has also been postulated to be caused by crystal regrowth from residual ESWL-derived particles that have found throughout the anatomical structure of the kidney (Köhrmann et al., 1993; Streem et al., 1996; Sun et al., 1996; Costa-Bauzá et al., 2005; Osman et al., 2005; Miller and Lingeman, 2007; Giannossi and Summa, 2010; Dawson and Tomson, 2012; Chongruksut et al., 2012; Zhong, 2013; Li et al., 2015; Khan et al., 2016; Kang et al., 2016; El-Assmy et al., 2019).

The present study was therefore undertaken to directly and experimentally quantify ESWL-induced kidney stone fragmentation from the perspective of an integrative geological, biological, and medical approach called GeoBioMed (Sivaguru et al., 2018, 2020, 2021; Saw et al, 2021; Fouke and Sivaguru, 2021). GeoBioMed includes utilization of an extensive literature base in the geosciences that present practical and theoretical approaches to characterizing and predicting grain size surface area reactivity. Six calcium oxalate (CaOx) stone fragments were collected from Mayo Clinic Patient 106 using standard percutaneous nephrolithotomy (PCNL) with shock pulse lithotripsy (SPL) procedures (Fig. 1), which are typically applied to stones greater than ~11mm in diameter (Keeley et al., 1999). These PCNL-derived fragments were further broken-down *ex vivo* on a Dornier Delta® III lithotripter to produce a wide array of smaller ESWL-derived particles. Weight loss during ESWL experimentation was determined ([PCNL-derived fragment weight] – [total ESWL-derived particle weight]) and size frequency distributions were measured from

reflected light images of loose ESWL-derived particles. A subset of these ESWL-derived particles were embedded in epoxy plugs with the polished surface analyzed using: (1) 250nm-resolution microscopy (reflected light – RL; brightfield – BF; ring aperture contrast – RAC; phase contrast – PC; polarization – POL; transmitted light photomultiplier tube - T-PMT; confocal autofluorescence - CAF); and (2) 140 nm-resolution microscopy (T-PMT; super-resolution auto-fluorescence – SRAF). Each epoxy plug was made into 25μm-thick doubly polished uncovered thin sections for 140nm-resolution microscopy (BF, POL, RAC, T-PMT, CAF). Mineralogy was determined with a combination of this high- and super-resolution microscopy and Raman spectroscopy. Results indicate that: (1) the original crystal growth, layering, and post-depositional alteration (*diagenesis*; altogether known as the *crystalline architecture*; Sivaguru et al., 2021) of CaOx kidney stones provide the essential contextual framework required to identify and track how ESWL fracture geometries develop; (2) ESWL-derived particle size frequency distributions can be effectively and systematically assessed using the geological Wentworth (1922) classification scheme; and (3) integration of these factors will significantly advance the ability to understand, predict, and ultimately prevent post-ESWL kidney stone recurrence.

CHAPTER 2
MATERIALS & METHODS

The experimental design and methodology applied in this study are summarized here and described in detail in the Appendix A: Supplementary Materials & Methods (Fig. 1). Kidney stone fragments were collected from one patient (Identifier Number 106) at the Mayo Clinic by A. E. Krambeck using PCNL and SPL. Medical history, standard serum labs, medication intake (e.g. citrate, thiazides, allopurinol), and comorbid conditions (e.g. diabetes mellitus, obesity, gout, hypertension, distal rental tubular acidosis, malabsorption-related conditions and diseases) were assessed from the medical record of Patient 106. Preoperative data included patient age, sex, BMI, prior surgical history, prior metabolic stone therapies, stone location based on CT scans, and stone density measurement. Metabolic panels, which included 24-hour urine collection and EQUIL2-calculated supersaturation, were completed one month before and after PCNL-interventions, as well as one and two years after (Tab. 1, 2). Six ~4-12mm-diameter PCNL-derived fragments (labeled 106F1-6) were collected and washed in deionized water, air dried, and imaged (Fig. 2A). Stone mineralogy was determined to be primarily calcium oxalate monohydrate (COM) using Raman spectroscopy and clinical micro-CT (3mm resolution) at the Mayo Clinic Metals Laboratories (Fig. 2B). This was confirmed with high- and super-resolution microscopy, high resolution micro-CT, and Raman spectroscopy analyses at the University of Illinois Urbana-Champaign (Illinois), additionally finding trace amounts of calcium oxalate dihydrate (COD). These PCNL-derived fragments were immediately placed in a -80°C dry shipper dewar and transported to the Carl R. Woese Institute for Genomic Biology (IGB) at Illinois. At the time of analysis, samples were thawed for 24 hours at room temperature.

Patient 106 consented and enrolled to have six PCNL-derived stone fragments analyzed, four of which were selected for this study (106F1-4; Fig. 1). Three-dimensional (3D) reflected-light imaging on the Zeiss AxioZoom.V16 and micro-CT scans at 3µm-resolution on a North Star Imaging X5000 were completed on stone fragments 106F1-4 in the IGB at Illinois (Fig. 3, 4). The micro-CT data was subsequently used to select the line of section and strategically orient, cut, and produce a doubly polished thin section from PCNL-derived fragment 106F3 exhibiting a complete cross-section of earliest-to-latest crystalline growth. PCNL-derived fragment 106F3 was three-dimensionally oriented, impregnated with epoxy, and made into ~60µm-thick, doubly polished, uncovered thin section (106F3-1) by L. Todorov at Buehler (Chicago, IL). The remaining epoxy-embedded sample that was cut from the thin section (106F3-2) was imaged on the Zeiss Axio Zoom.V16 and sent to Wagner Petrographic to be prepared into a standard-sized (24mm x 46mm), uncovered (no cover slip), doubly polished thin section. Thin section microscopy analyses on 106F3-1 were carried out in the Microscopy and Imaging Core Facility in the Carl R. Woese Institute for Genomic Biology on a Zeiss Axio Zoom.V16, AxioScan.Z1, Axio Observer, and LSM 880 Confocal system before being sent out to Wagner Petrographic for final polishing to ~25µm thickness. After receiving both 106F3-1 and 106F3-2 thin sections from Wagner Petrographic, image analyses were carried out using the Zeiss AxioScan.Z1 and LSM 980 Confocal microscopes (Fig. 3, 5, 6).

PCNL-derived fragment 106F1 was sacrificed for experimental standardization and PCNL-derived fragments 106F2 and 106F4 were used for the ESWL experimentation on the Dornier Delta® III lithotripter. In preparation for ESWL experimentation, two PCNL-derived fragments (106F2, 106F4) were saturated with 72-hour degassed 18.2 MilliQ H2O for 24 hours within a vacuum chamber (McAteer et al., 2005). The lithotripter was set to a rate of 90 shocks/min

in increments of 100 shocks per treatment, with a coupling pressure of 4, and a power level of 3. Samples were placed in a calibration chamber attached to the ESWL instrument. This configuration mimics penetration of the shock waves through human tissue and focused shockwaves at the center of a 2mm-mesh net containing the sample. After each 100-shock treatment, ESWL-derived particles sieved within the 2mm-mesh net and ESWL-derived particles that fell through the 2mm-mesh net were separately collected and photographed. The water bath containing the fallen ESWL-derived particles was extracted and filtered using a 0.47μm mixed cellulose ester membrane filter paper within a vacuum system. The ESWL-derived particles within the 2mm-mesh net were removed, weighed, then returned for subsequent treatments (Fig. 7). The procedure was repeated until all fragments in the 2mm-mesh net were completely fragmented. Weight loss during ESWL experimentation was determined ([PCNL-derived fragment weight] – [total ESWL-derived particle weight]) and size frequency distributions were measured from reflected light images of loose ESWL-derived particles.

ESWL-derived particles from 106F2 and 106F4 were collected from the calibration container water bath after each 100-shock ESWL treatment, placed into a weigh boat, and imaged on a Zeiss Axio Zoom.V16 microscope. Image analysis was completed using Adobe Photoshop and RGB false colored (red = 210, green = 0, blue = 255) to ensure accurate grain size quantification (Fig. 8). Each image was then processed using the Zeiss AxioVision program, with the total number of fragments and measured diameters converted into XML and XLSX files. Data was evaluated on Microsoft Excel and binned according to the Wentworth grain size scale. Size frequency distributions could only be determined from loose ESWL-derived particles because thin sections made from epoxied ESWL-derived particles can significantly under sample the grain sizes due to the polishing-impact on the elevation of the plane of section. ESWL-derived particles from

106F2 and 106F4 collected during the first ESWL 100-shock treatment were embedded in epoxy blocks, imaged on Zeiss AxioZoom.V16, Axio Observer, and LSM 880 Confocal microscopes. Impregnated blocks were then shipped to Wagner Petrographic Ltd. (Linden, Utah) for preparation as ~25µm-thick, uncovered, doubly polished thin sections. Received thin sections of 106F2-S1 and 106F4-S1 were then imaged on the Zeiss AxioScan.Z1, LSM 880 Confocal, and LSM 980 Confocal microscopes for further analysis (Figs. 9-16).

Both epoxy-embedded plugs and thin sections were imaged on a wide variety of optical modalities. A Zeiss Axio Zoom.V16 system (Carl Zeiss, Oberkochen, Germany) with a Plan-NeoFluar Z 1.0x objective and Axiocam 512 imaging device for reflective and transmitted light microscopy, including brightfield (BF) and polarization (POL) images. A Zeiss AxioScan.Z1 system with a Plan-Apochromat (10x/0.45 NA) objective and Hitachi HV-F202SCL imaging device was used to capture BF, POL, and ring aperture contrast (RAC). A Zeiss Axio Observer system with a Zeiss Axiocam 506 imaging device was used to capture BF, POL, and phase contrast (PC) images across a broad range of magnifications (10x: 0.45 NA; 20x: 0.8 NA; and 63x: 1.4 NA). The objectives used were Plan-Aprochromat (10x/0.45NA) Ph1 M27 DICII, Plan-Aprochromat (20x/0.80 NA) Ph2 DICII, and Plan-Aprochromat (63x/1.40 NA) Oil Ph3. For POL images, Analyzer DIC Trans.Light reflector was utilized with polarizer set to 0°. The confocal auto-fluroescence (CAF) and Airyscan super-resolution autofluorescence (SRAF) nanolayers observed in the samples were investigated and quantified using both the Zeiss LSM 880 and Zeiss LSM 980 Laser Scanning microscopes with Airyscan super-resolution. Tiled CAF images of merged pseudo-colored RGB channels exhibits a complete history of earliest-to-latest stone growth crystallization.

All images were processed using the Zeiss Zen Blue and/or Black software to display either minimum and maximum or best-fit properties unless otherwise stated in the figure legends. In addition, red-green-blue (RGB) curves were adjusted individually or together to highlight all the crystal intensities in individual frames across the whole specimen. Where required, a non-linear gamma correction of 0.45 or 0.70 was applied to enhance faint AF crystal intensities in the same Zen program under the spline display mode property and all other corrections are presenting in the corresponding figure legends. Final images were cropped, resized, and assembled using Adobe Photoshop (Adobe Systems Inc., San Jose, CA) to fit the required format.

CHAPTER 3
RESULTS & DISCUSSION

CRYSTALLINE ARCHITECTURE OF PCNL-DERIVED FRAGMENTS

The high- and super-resolution optical, laser, and x-ray microscopy and spectroscopy conducted in the present study indicates that the original PCNL-derived fragments exhibit crystalline architectures consistent with those previously observed and described in CaOx kidney stones (Sivaguru et al., 2018, 2020, 2021; Saw et al., 2021). As used herein, the term "crystalline architecture" includes stone structure (crystal size, shape, intergrown morphologies), stratigraphy (crystal layering), diagenetic phase transitions (post-depositional dissolution and recrystallization), and paragenesis (historical sequence of formational events). Therefore, the approaches and terminology of GeoBioMed (as presented in Sivaguru et al., 2018, 2020, 2021) have been adopted and directly applied in the following descriptions. RL microscopy and x-ray micro-computed tomography (micro-CT) indicate that the original PCNL-derived fragments are irregular ~4-12mm-diameter crystalline aggregates that exhibit SPL probe impressions and breakage patterns (Figs. 2, 3A, B, 4). Each PCNL-derived fragment is primarily a high-density calcium oxalate monohydrate (COM; Whewellite; CaC2O4 • H2O) cortex (COM_C) composed of high-frequency alternations of organic-matter-rich (peptides, proteins, and other cellular molecules) and COM mineral-rich nanolayers (Figs. 3B-F; Khan et al., 1986, Pittomvils et al, 1993; Roberts and Resnick, 1986, McLean and Nickel, 1994). All six of the PCNL-derived fragments were impacted to varying degrees by ultrasonic wave energy and intermittent shockwaves from use of an SPL probe. This includes breakage surfaces and notch formation on the exterior of some PCNL-derived fragments (Figs. 2, 3A, B, 4), as well as rare occurrences of fine fracturing within COM_C that are exclusively observed adjacent to the SPL notches (Fig. 6A).

Individual crystal faces (sector zones) within COM_C are common and form as the result of disequilibrium precipitation, during which ions and organic matter are differentially incorporated on age-equivalent crystal growth faces (Figs. 6B, C, H; Dowty, 1976; Sivaguru et al., 2018, 2020, 2021; Saw et al., 2021). Free-floating COM crystals (COM_{FF}) are entombed, either individually or in clusters, on growing COM_C concentric surfaces that seed the growth of radiating crystal bundles (COM_B) that either truncate or redirect the growth of sector zones (Figs. 6C, F). Additionally, COM_C commonly exhibits repeated *in vivo* events of crystal fracturing (cracking) and faulting (displacement across the fractures) to form laths with discontinuous layering (Figs. 6D, E). COM_C also exhibits Ångstrom-scale dissolution and recrystallization (mimetic replacement, COM_M) (Figs. 6E, G). The outermost margins of the PCNL-derived fragments are composed of calcium oxalate dihydrate (COD; Weddellite; CaC2O4 • 2H2O) crystals that were encrusted by COM_C, experienced COD dissolution (COD_D), and were partially filled with replacement COM (COM_R) (Fig. 6H).

FRACTURE GEOMETRIES OF ESWL-DERIVED PARTICLES

The crystalline architecture of the ESWL-derived particles, as revealed by CAF and SRAF microscopy, provides a high-fidelity crystalline framework within which to characterize ESWL-induced fracture geometries (Figs. 12, 14). Importantly, previous studies using scanning electron microscopy (SEM) on ESWL-derived particles provided valuable information on external and internal CaOx crystal growth and fracturing morphologies (Kahn et al., 1986). However, the SEM tool is inherently limited compared to the crystalline architecture that is provided by the CAF and SRAF microscopy (Sivaguru et al., 2018, 2020, 2021; Saw et al., 2021). ESWL-induced fractures were observed in the present study to propagate in a variety of perpendicular, oblique, and

concentric-parallel trajectories relative to the nanolayered crystalline architecture of the original PCNL-derived fragments (Figs. 9-16). These observations have been integrated to establish a systematic nomenclature of fracture morphologies for ESWL-derived particles that include: (1) rectangular particles with fracture margins formed perpendicular to the COM_C concentric nanolayer stratigraphy (Fig. 12A), parallel to radiating sector zones (Figs. 14B, D), and cut through COM mimetic replacement (COM_M) crystals (Figs. 14G) (Dugdale, 1960; Barenblatt, 1962; Lokhandwalla and Sturtevant, 2000; Kahn et al., 1986); (2) pointed particles that form from fractures perpendicular, oblique, and parallel to the COM_C concentric nanolayer stratigraphy (Figs. 12B-H) and merge at angles of 60-120° to form arrowhead-like tips (Figs. 12B-H, 14A, D) that are similar in appearance to Hertzian-cone conchoidal fractures caused by surface radial tensile stress in silicates and metals (Lokhandwalla and Sturtevant, 2000; Chaudri, 2015; Bilgren et al., 2018); (3) concentrically spalled particles created by intercrystalline and/or intracrystalline fracturing along concentric organic matter-rich COMC nanolayers via cohesive-zone brittle microfracture spallation (Figs. 12F, G) (Dugdale, 1960; Barenblatt, 1962; Zhong, 2013); and (4) irregular surface particles created by coalescing microfractures that cause irreversible fatigue damage and little plastic deformation during the application of cyclic tensile stress (Dugdale, 1960; Barenblatt, 1962; Kachanov, 1986; Lokhandwalla and Sturtevant, 2000; Rassweiler et al., 2011) at the margins of original COM crystal bundles that initially grow from COM free floating (COM_{FF}) after landing on growing COM_C surfaces (Figs. 14B-H). These fracture categories enhance and improve upon observations completed in earlier studies exclusively using SEM (Kahn et al., 1986) as a result of the CAF and SRAF microscopy utilized in the present study.

ESWL-DERIVED PARTICLE SIZE DISTRIBUTION

During the course of the 72-hour H_2O porosity saturation of the original PCNL-derived fragments (McAnteer et al., 2005), the weight of both 106F2 and 106F4 increased ~10% (Fig. 17A). The larger PCNL-derived fragment 106F2 was exposed to six sequential *ex vivo* 100-shock ESWL treatments with a consistent Level 3 intensity at a rate of 90 shocks per minute (Fig. 17). The smaller PCNL-derived fragment 106F4 was subjected to only two 100-shock ESWL treatments at the same shockwave intensity and rate (Fig. 17). The ESWL-derived particles produced by each 100-shock ESWL treatment were sieved with the 2mm-mesh net in the calibration container of the lithotripter, weighed, and imaged (Fig. 7; Tab. 3). The weight percent of ESWL-derived particles captured in the 2mm-mesh net was observed to decrease from ~50-85% after the first 100-shock ESWL treatment, to eventually reaching a 0% decrease after progressive treatments (Fig. 17A). This is consistent with previous observations of weight loss with increasing shock wave treatments (Pittomsvils et al., 1999). The ESWL-derived particle fractions small enough to pass through the 2mm-mesh net were trapped on a 0.47μm filter, imaged, quantified, and classified according to the Wentworth grain size scale (Wentworth, 1922; Reihl Jr. et al., 1987; Maxwell et al., 2015; Figs. 17B, C). These analyses indicate that the ESWL-derived particles from both 106F2 and 106F4 that passed through the 2mm-mesh net are in size classes that range from very fine silt (4.998μm) to very fine pebbles (2.926mm) (Figs. 17B, C; Tab. 4). The ESWL-derived particles from both 106F2 and 106F4 exhibit right-skewed (positive) normal size frequency distributions (after Garcia, 2008) and modes of fine sand sized classes (Figs. 17B, C). Importantly, while the smallest clay-sized fraction could not be captured and analyzed given the techniques used in the present study (Fig. 17B, C), some unknown amount of this size class was undoubtedly produced during the sequential stages of ESWL experimentation.

CHAPTER 4
IMPLICATIONS

Clinical micro-CT imaging consistently, safely, and non-invasively permits the *in vivo* detection of kidney stones and their ESWL-produced fragments and particles down to a detection limit of 3-4mm in diameter (Du et al., 2007). Micro-CT imaging therefore serves as a fundamentally important diagnostic tool for determining the effectiveness of ESWL treatments in symptomatic patients (Duan et al., 2013). This has led some clinicians to go so far as to use negative micro-CT screens to identify patients as "kidney stone free" with "clinically insignificant residual fragments" that include "residual 'sandy' fragments" (1-4mm-diameter particles) and "dust" (1mm-daimeter particles; Moon et al., 1993; Street et al., 1996; Zanetti et al., 1997; Shigeta et al., 1999; Fialkov et al., 2000; Tan and Wong, 2005; Osman et al., 2005, Hyams et al., 2010, Dincel et al., 2012; Kang et al., 2016, Brian et al., 2021). In contrast, results of the ESWL experimentation presented in the present study indicate that each 100-shock ESWL treatment produces 100s of 5-2000μm-diameter particles that range on the Wentworth size scale from very fine silts through sands and very fine pebbles, with a mode grain size of 125-250μm-diameter particles (Figs. 17B, C). In addition, the collection techniques used in the present study could not capture clay-sized particles that are also likely present within the ESWL-derived particle size range (Figs. 17B, C). Importantly, nearly all these ESWL-derived particles are below the 3-4mm-diameter detection limit of clinical micro-CT (Fig. 18). Yet as presented in the following evaluations, the presence and abundance of these ESWL-derived particles are likely to have a significant impact on influencing the high 50% rate of post-ESWL stone recurrence within 10 years (Uribarri et al., 1989; Kamihira et al., 1996; Fialkov et al., 2000; Khaitain et al., 2002).

Documentation of size frequency distribution of the particles produced by ESWL treatments (Fig. 18) permit quantitative estimates of the effect of the entire range of grain size distributions on chemical reactivity (Berner, 1980; Lasaga et al., 1981) and ensuing post-ESWL recurrence. The increase in surface area as grain size and volume decreases can be approximated as:

$$A = \frac{\lambda}{(\rho * V)} = \frac{\beta}{\rho}(r^{-1})$$ (Walter and Morse, 1984) where:

A = specific surface area (SSA_p) of particle per unit mass (g)

λ = particle surface area (also known as A_p) per unit mass (g) – function of equivalent spherical radius (r): $A_p = 4\pi r^2$

V= volume of each particle (also known as V_p) as a function of equivalent spherical radius (r): $V_p = \frac{4}{3}\pi r^3$

ρ = bulk density of material (COM) = 2.12 g/cm3

β = shape factor for sphere or cube = 3 (unitless)

This permits the effect of particle size and surface area to be considered in the context of surface-control versus transport-control chemical reactivity regimes (Fig. 18; Berner, 1980; Lasaga et al., 1981). As a result, the entire range of ESWL-derived particle sizes (Figs. 17C, D), while below clinical micro-CT detection (Fig. 18), all possess an extremely high potential to form as a nidus for stone regrowth and recurrence (Grover et al., 2002). In addition, the extremely small size of these fine ESWL-derived particles (Figs. 17C, D, 18) indicates they would be trapped within the boundary layer (Vogel 1996) of urine flow across the surfaces of tissues and cells, and therefore extremely difficult to remove with post-ESWL irrigation (Keeley et al., 1999; Kang et al., 2016). This supports the suggestion by Brain et al. (2021) that smaller size particles should not

be discounted because with increasing time there is increasing risk of recurrence. Therefore, terms such as “clinically insignificant fragments” should be abandoned.

Shock wave lithotripsy, which has been in clinical use since the 1980s, has spurred extensive controlled experimentation to better understand the mechanisms of fragmentation, improve efficiency of the treatment, and reduce post-ESWL stone recurrence (Wess and Mayer, 2020). The majority of this work has been completed on artificial composites (BegoStones or phantom stone analogs) suspended in water (Eisenmenger, 2001; Liu and Zhong, 2002; Mota and Ortiz, 2006; Pishchalnikov et al., 2006; Sapozhnikov et al., 2007; Qin et al., 2010; Smith and Zhong, 2012; Lautz et al., 2013; Maxwell et al., 2015). Furthermore, other studies have shown that COM is more resistant to ESWL-generated fragmentation compared to COD (Pittomvil et al., 1994). However, this previous work did not incorporate kidney stone crystalline architecture (versus “physical properties” without crystalline structure), size frequency distributions (versus acoustic comminution base on averages), and the influence on ESWL fracturing and recurrence. The original crystalline architecture of each PCNL-derived fragment that was subjected to ESWL treatment in the present study indicate ESWL-induced fracture propagation produces a variety of geometric orientations. These included rectangular, pointed, concentrically spalled, and irregular ESWL-derived particles. Similar to arrow heads produced from chert, these irregularly shaped particles have razor sharp edges that can cut into and damage sensitive tissues throughout the kidney, bladder, and urethra, which will further contribute to ensuing stone recurrence (Sivaguru et al., 2021).

CHAPTER 5
CONCLUSION

The results of the present study reveals immense new possibilities to experimentally study processes that might disrupt diagenetic phase transitions driven by ESWL-derived particles, which will lead to kidney stone regrowth and recurrence. This includes not only the study of nucleation phenomena, but also the possibility for *in vivo* dissolution and determination of the effective concentrations and combinations of previously identified inhibitors and promoters of kidney stone growth (Sivaguru et al., 2021). These can be tested at each stage of the paragenesis controlling recurrence to identify and develop previously unexplored therapeutic interventions, as well as require systematic controlled experimentation in a microfluidic testbed called the GeoBioCell (Sivaguru et al., 2018, 2021; Saw et al., 2021; Fouke et al., 2022).

The GeoBioCell can be used to systematically test and study the influence of microbiome-derived and host-human-derived protein catalysis by macromolecules and other effects on crystal growth, aggregation, and diagenetic alteration, including real-time dissolution and recrystallization events (Sivaguru et al., 2021). This could include testing of specific bacteria and fungi previously identified as being entombed in and have metabolic activity impacting kidney stones (Saw et al., 2021), as well as those shown to dissolve minerals in natural and engineered environments via excretion of a number of organic acids, such as citric, oxalic and formic acids. To complete this, new GeoBioCells can be designed and constructed with 3D printing and silica etching of microfluidic flow channels in multiple configurations to simulate the actual hydrology, anatomy, and physiology of the human kidney. To further simulate the *in vivo* environment, living kidney cell lines can be 3D printed within the GeoBioCell (Sivaguru et al., 2021). For example, effects of dosing and specific plant extracts and antioxidants such as hydroxycitrate could be tested with

respect to nucleation, crystallization, dissolution, recrystallization and effect on development of specific crystalline architectures (Micali et al., 2006; Tang et al., 2006). This could be conducted with respect to factors such as cellar control, urine supersaturation influence, and flow rate (Sass et al., 1991; Grover et al., 2002; Costa-Bauzá et al., 2006; Hsi et al., 2017). Experiments can be completed on PCNL-derived fragments and ESWL-derived particles within specific size frequency distribution (Figs. 17C, D, 18). Examples could include testing of the concentration dependence and the effect of specific drugs and inhibitors, such as anionic proteins and glycosaminoglycans, on crystal aggregation and cell attachment (Roberts and Resnick, 1986; Costa-Bauzá et al., 2005; Pfau and Knauf, 2016; Zisman, 2017; Sivaguru et al., 2021). The effectiveness of each clinical intervention strategy would be systematically tested via GeoBioCell experimentation. Experiments could also be designed to establish the relative degree of chemical reactivity for each Wentworth grain size class produced by differing ESWL intensity and frequency settings

CHAPTER 6
FIGURES & TABLES

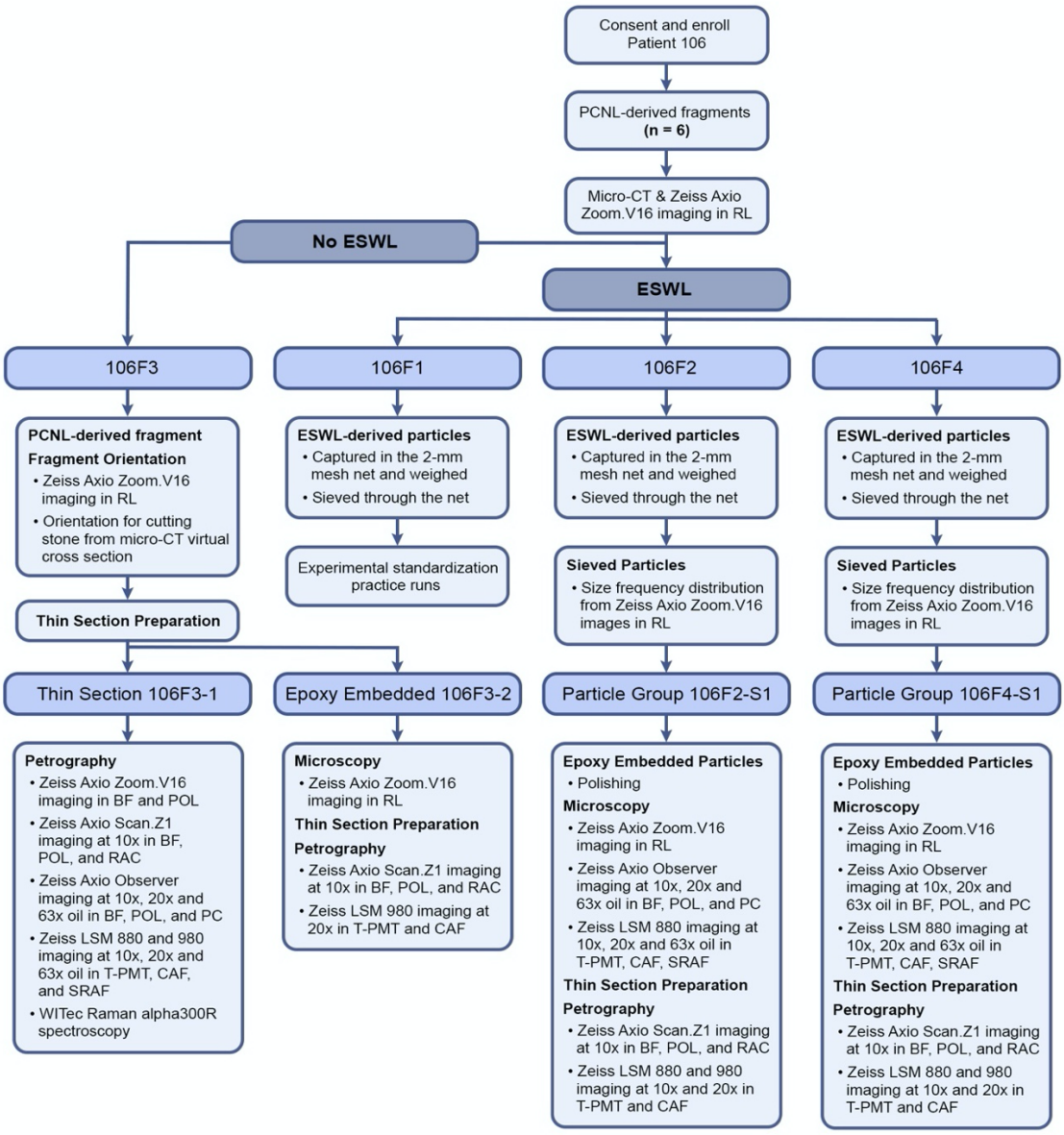

Figure 1. Flow chart of experimental study (see explanation in Supplementary Materials and Methods). Acronyms include: PCNL, percutaneous nephrolithotomy; micro-CT, micro-computed tomography; RL, reflected light; BF, brightfield; POL, polarization; RAC, ring aperture contrast; PC, phase contrast; T-PMT, transmitted light photomultiplier tube; CAF, confocal autofluorescence; SRAF, super-resolution autofluorescence; and 10X, 20X, 63X, microscope objective magnification.

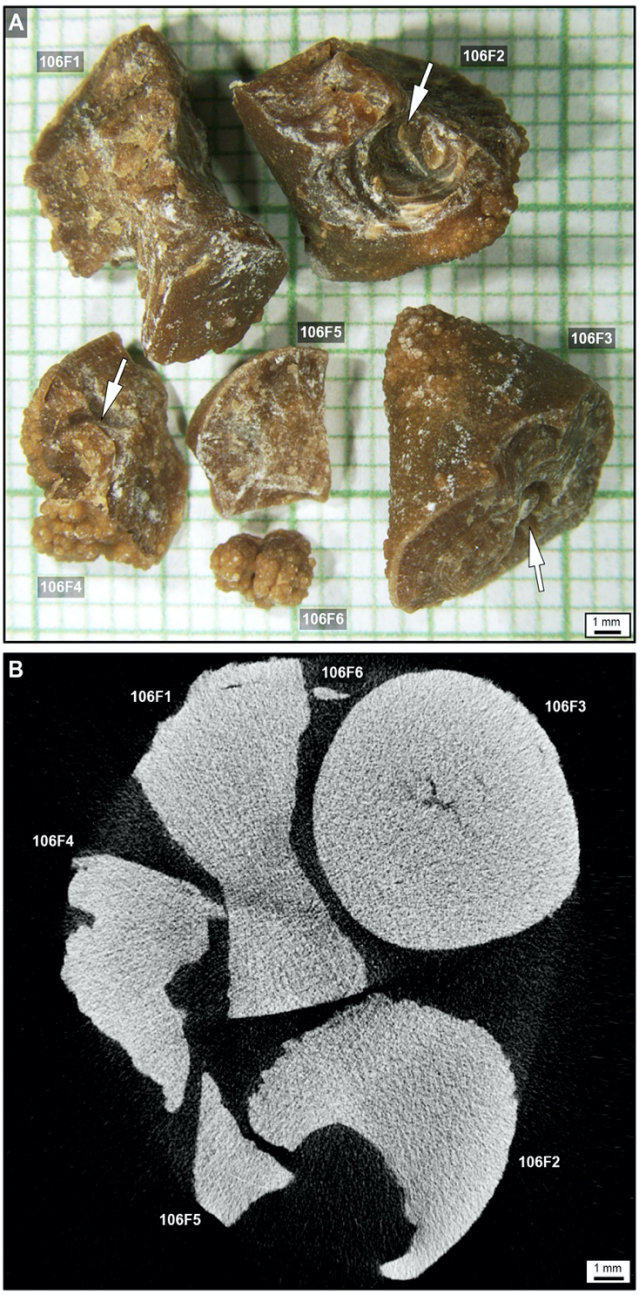

Figure 2. Six PCNL-derived fragments from Patient 106 from the Mayo Clinic. The major axis (longest diameter) for each fragment is: 106F1, 11.47 mm; 106F2, 11.51 mm; 106F3, 11.67 mm; 106F4, 8.36 mm; 106F5, 6.31 mm; and 106F3, 4.08 mm. (A) RL image of PCNL-derived fragments 106F1-6 taken at the Mayo Clinic. (B) Micro-CT image of PCNL-derived fragments 106F1-6 taken at the Mayo Clinic. PCNL-derived fragments 106F1-4 were used in the present study. White arrows show notches resulting during PCNL SPL procedure.

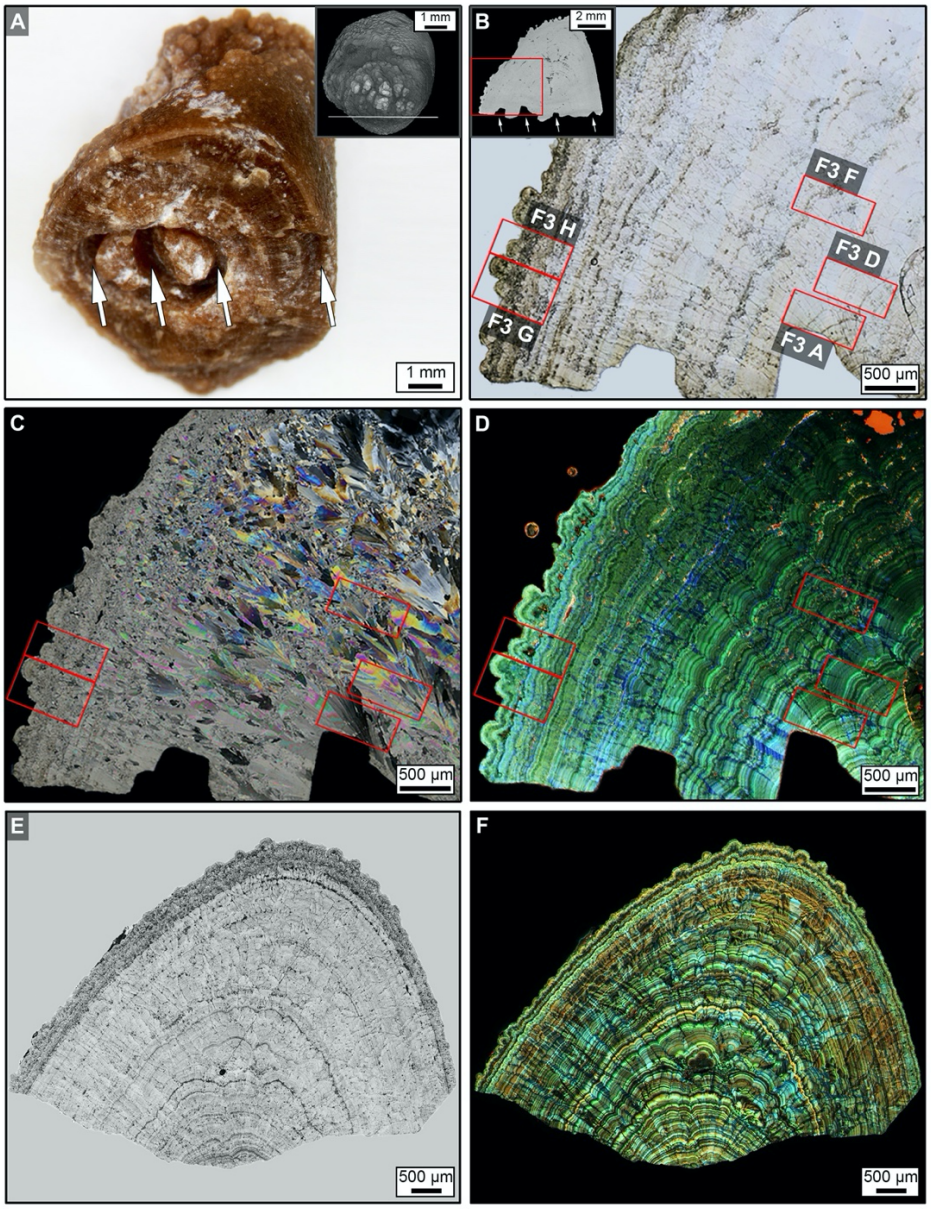

Figure 3. Three-dimensional (3D) external morphology of kidney stone fragment 106F3 and two-dimensional (2D) internal crystalline architecture of thin sections 106F3-1 and 106F3-2. (**A**) 3D reflected light (RL) image of the entire stone showing notches (white arrows) resulting during PCNL SPL procedure. Weight data presented in Table 3. Inset is a 3D microcomputed tomography (micro-CT) external surface rendering of entire stone from a different orientation showing the line of section (white line). Thin section 106F3-2 was prepared ~500 µm below the line of section. (**B**) Brightfield (BF) image of 2D virtual thin section 106F3-1 made at position

shown in the line of section show in the inset of **A**, exhibiting a complete history of earliest-to-latest stone growth crystallization. Red boxes indicate the locations of enlargements shown in Figure 6. Inset is a 2D virtual micro-CT cross-section taken through line of section shown in **A**. White arrows show PCNL SPL notches that correspond to **A,** and red box indicated enlargement in **B**. (**C**) Polarization (POL) image of **B**. Red boxes indicate the location of enlargements shown in Figures 3C and 6. (**D**) Tiled confocal autofluorescence (CAF) image of merged pseudo-colored red, green, and blue (RGB) channels indicate that the COM cortex (COM_C) is composed of nano-layering. Red boxes indicate the location of enlargements shown in Figures 3C and 6. (**E**). T-PMT of thin section 106F3-2 exhibiting the original internal crystalline architecture of the PCNL-derived 106F3 stone fragment. (**F**) Tiled CAF image of merged pseudo-colored RGB channels of **E**.

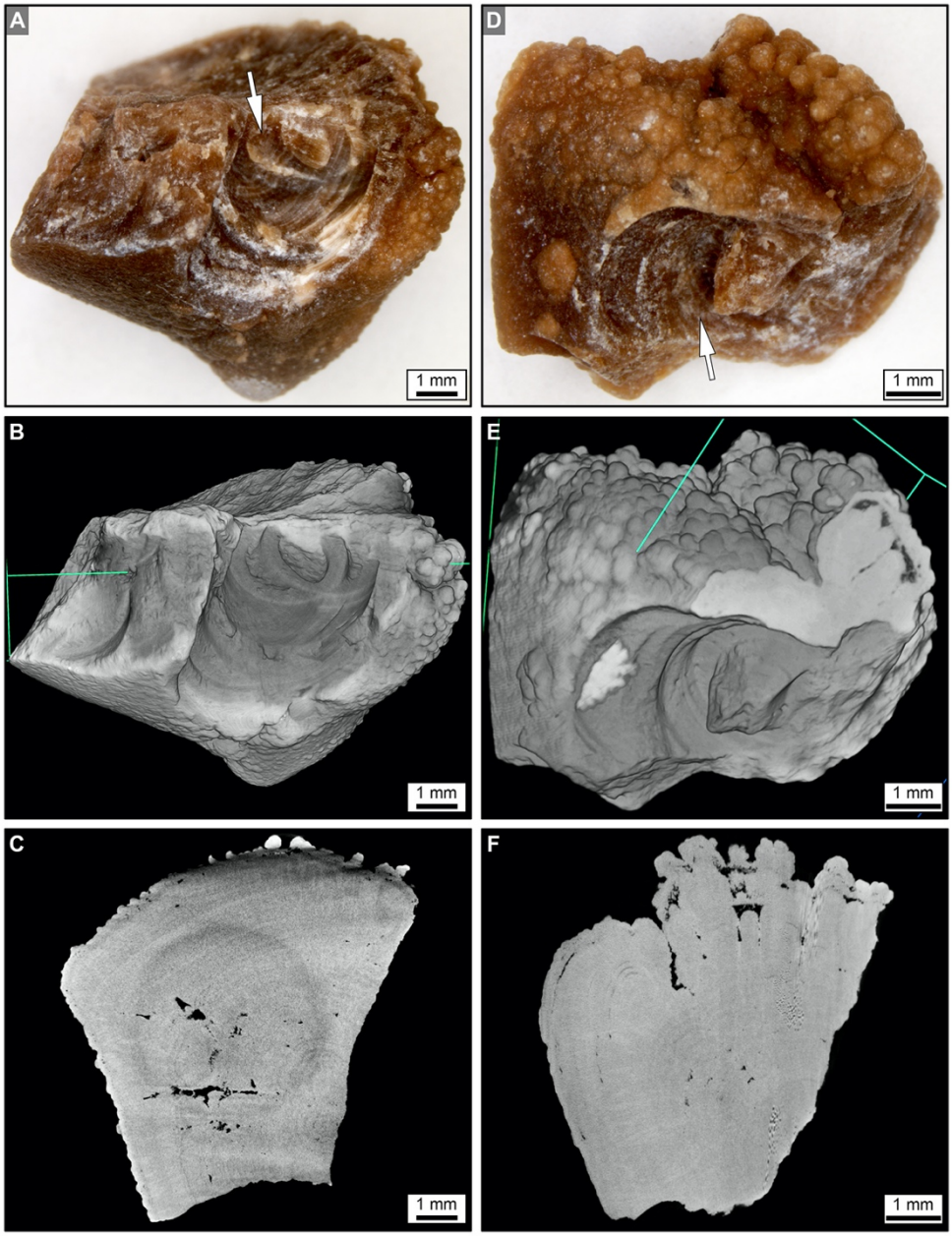

Figure 4. Three-dimensional (3D) external morphology and two-dimensional (2D) internal crystalline architecture of PCNL-derived fragments 106F2 (**A**-**C**) and 106F4 (**D**-**F**) prior to experimentation. (**A, D**) 3D RL image of the entire stone showing notches (white arrows) resulting during PCNL SPL procedure. (**B**, **E**) 3D micro-CT of the external surface rendering of the entire stone. (**C**, **D**) 2D virtual micro-CT cross-section of the internal crystalline structure. Complementary figure of stones during experimentation presented in Figures 7 and 8.

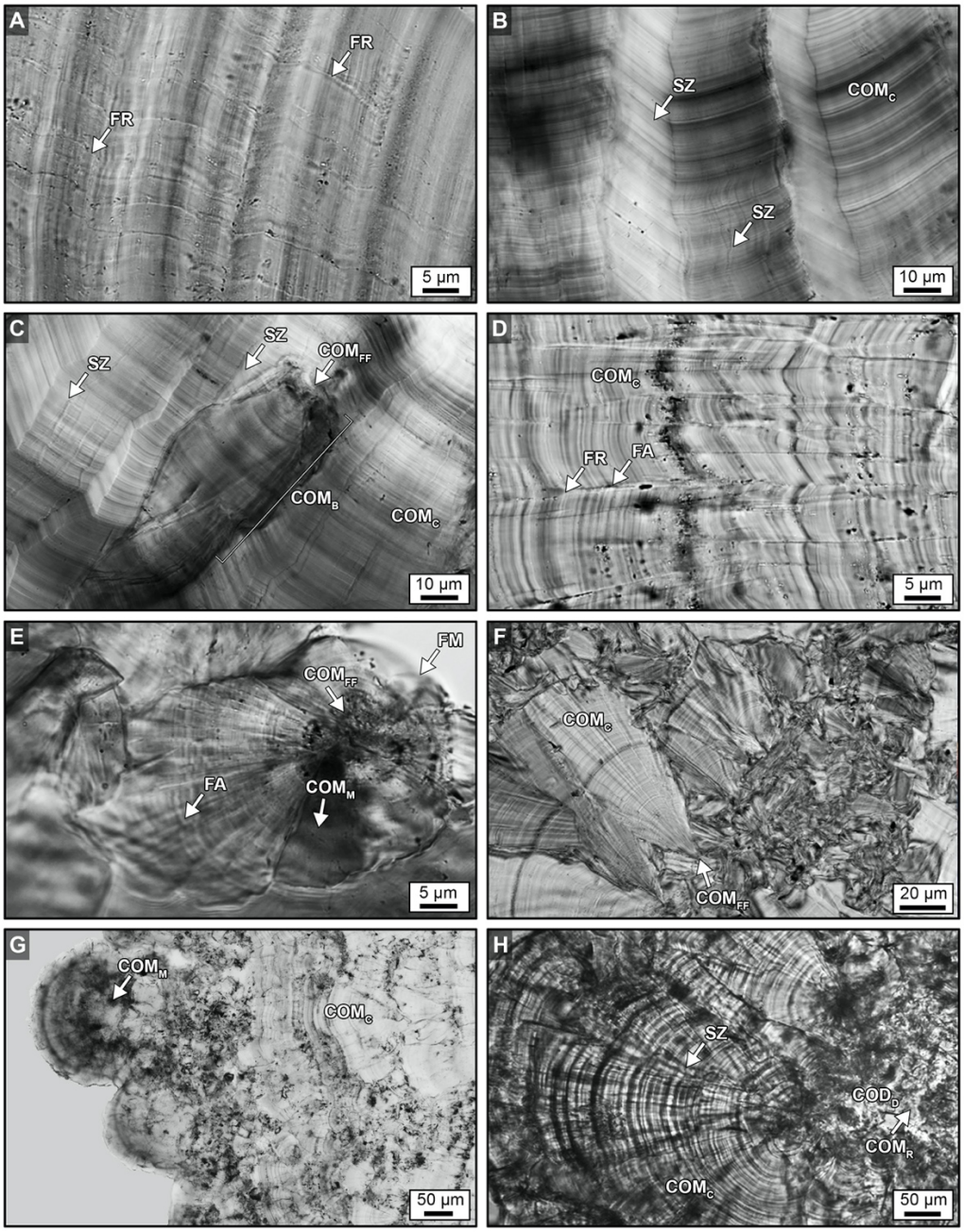

Figure 5. Original crystalline architecture of CaOx PCNL-derived fragments. (**A-H**) T-PMT images. Labels indicate: FR, fracture; FA, fault; SZ, sector zone; COM_{FF}, free-floating COM; COM_C, COM cortex; COM_B, bundles of COM radiating from a COM_{FF}; COM_M, mimetic replacement COM; COM_R, replacement COM; and COD_D, dissolved COD. Complementary CAF and SRAF images presented in Figure 3. Image locations shown in Figures 3C, D and 8C and complementary SRAF and CAF images presented in Figure 6.

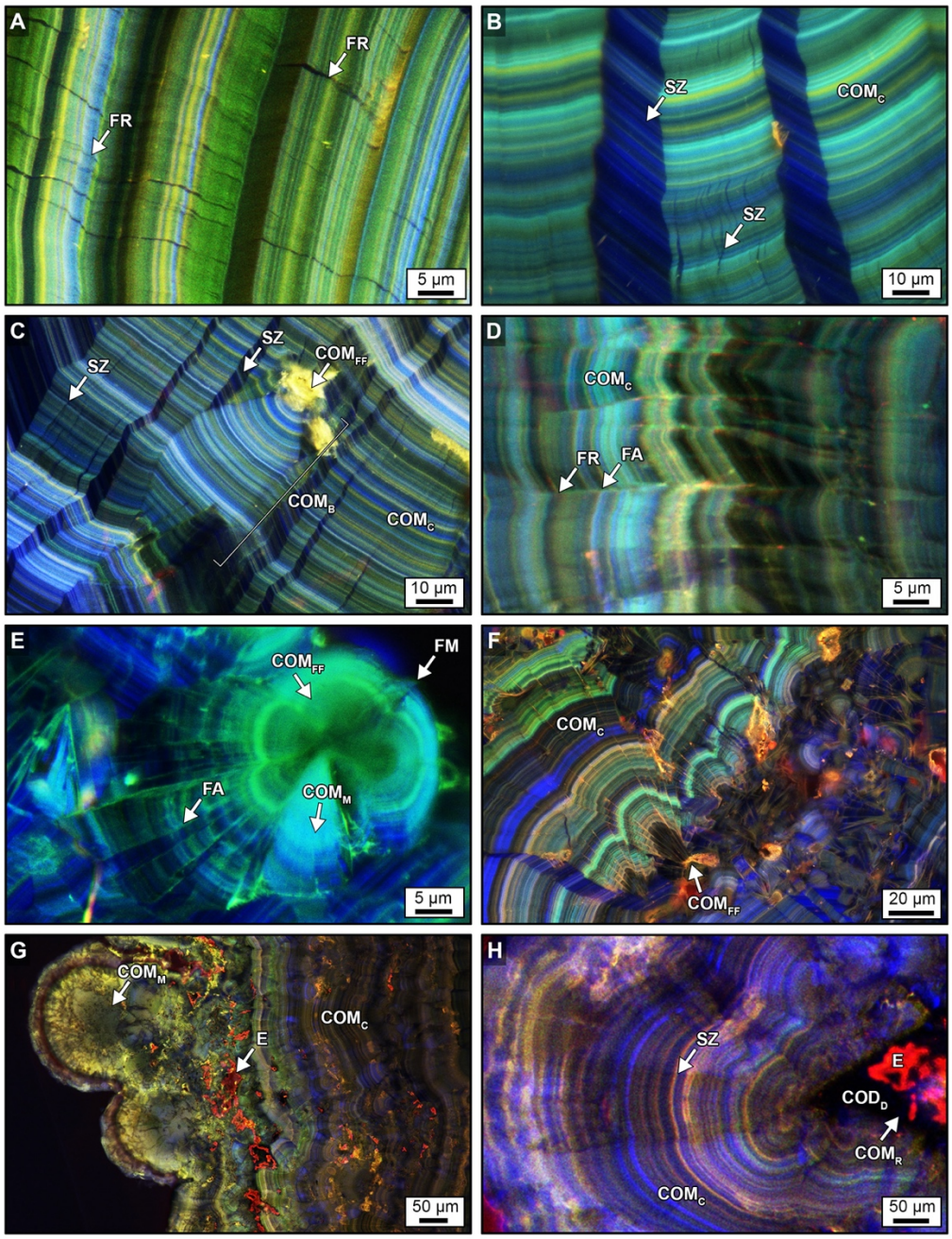

Figure 6. Original crystalline architecture of calcium oxalate (CaOx) PCNL-derived fragments. (**A, D, E**) SRAF images. (**B, C, F, G, H**) CAF images. Labels indicate: FR, fracture; FA, fault; SZ, sector zone; COM_{FF}, free-floating COM; COM_C, COM cortex; COM_B, bundles of COM radiating from a COM_{FF}; COM_M, mimetic replacement COM; COM_R, replacement COM; COD_D, dissolved COD; and E, red AF embedding epoxy. Image locations shown in Figures 3C, D and 8C and complementary T-PMT images presented in Figure 5.

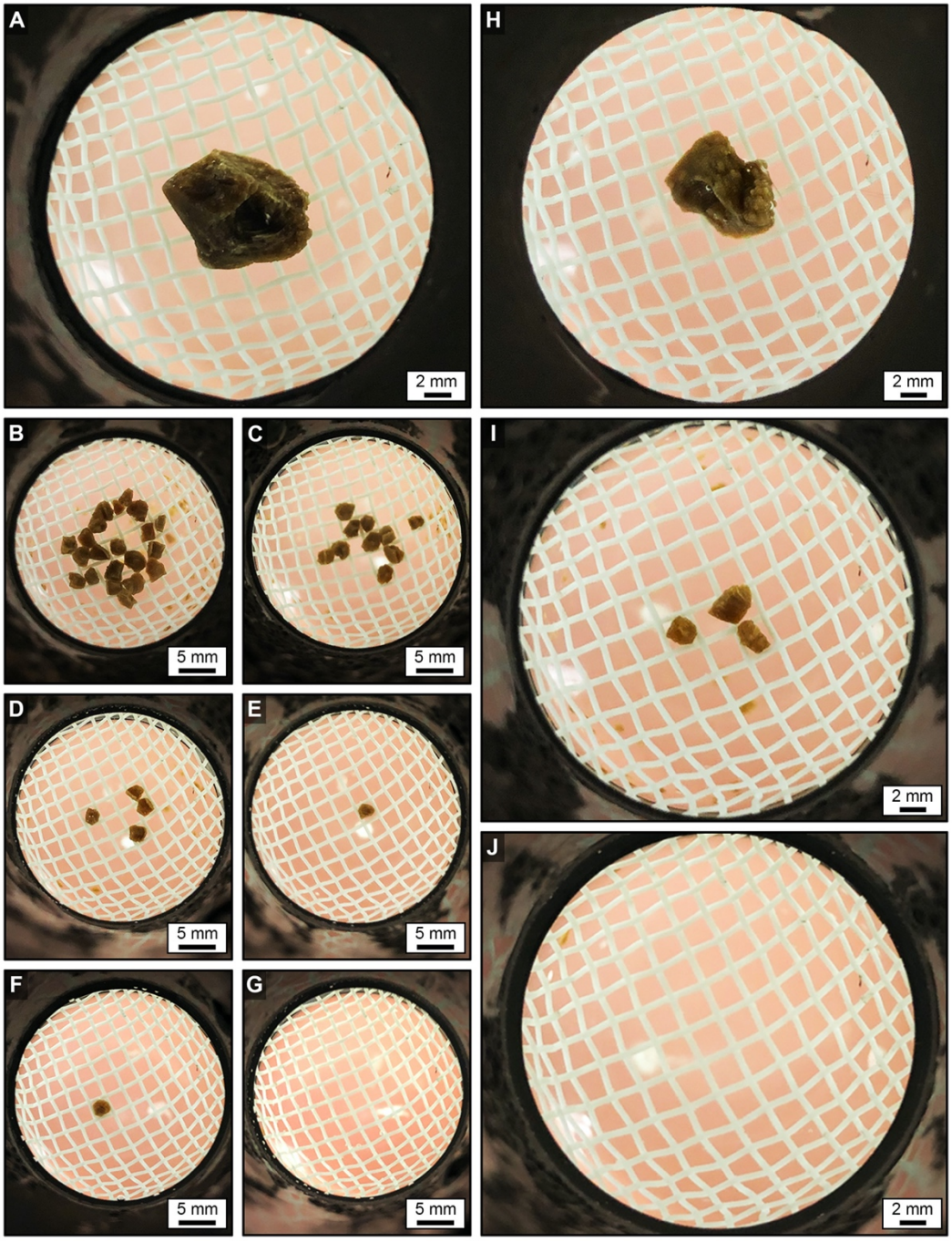

Figure 7. Weight changes of ESWL-derived particle groups 106F2 (**A**-**G**) and 106F4 (**H**-**J**) suspended within 2 mm-mesh net. (**A**, **H**) RL images of PCNL-derived fragment prior to experimentation. (**B**, **C**, **D**, **E**, **F**, **G**, **I**, **J**) RL images of ESWL-derived particles during experimentation. Complementary images presented in Figure 4 and 8A, D and data is presented in Figure 17A and Table 3.

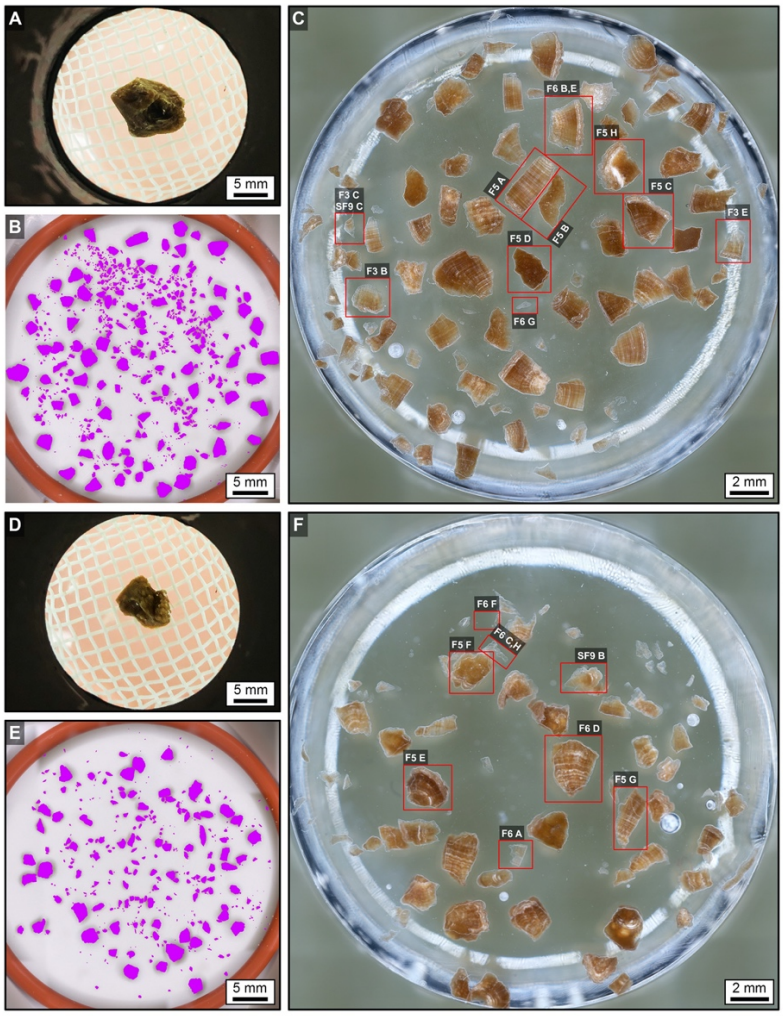

Figure 8. PCNL-derived fragments 106F2 (**A**) and 106F4 (**D**) that were shocked with ESWL to produce particle groups 106F2-S1 (**B**, **C**) and 106F4-S1 (**E**, **F**). Particles derived from the first 100 ESWL shocks were imaged (**B**, **E**) and embedded in an epoxy plug (**C**, **F**). (**A**, **D**) RL image of PCNL-derived fragment suspended within a 2 mm-mesh net basket prior to ESWL treatment. Complementary figures of 3D external stone morphology, 2D internal crystalline structure, and RL images during experimentation presented in Figures 4 and 7. (**B**, **E**) RL image of loose ESWL-derived particles that were hand-traced and artificially colored pink for precise pixel selection and grain size quantification. (**C**, **F**) RF image of ESWL-derived particles embedded in epoxy and polished prior to thin section preparation (red boxes indicate locations of enlargements shown in Figures 6, 12, 14, and 16.

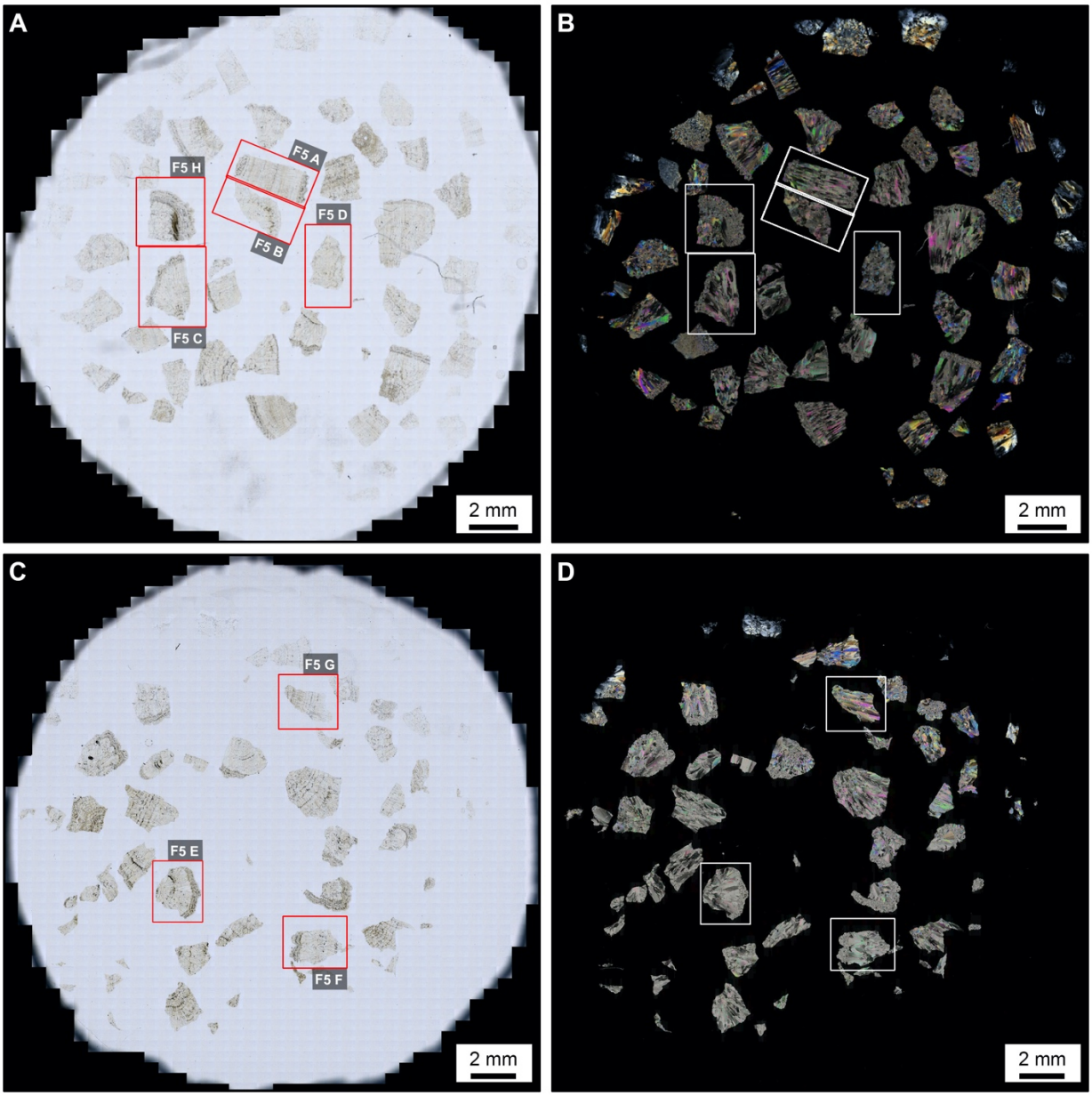

Figure 9. Geometries of ESWL-derived particles from groups 106F2-S1 and 106F4-S1 (shown in Fig. 5) that were thin sectioned. (**A, C**) BF images. (**B, D**) POL images. Complementary CAF, BF, and POL images presented in Figures 10, 11, and 12.

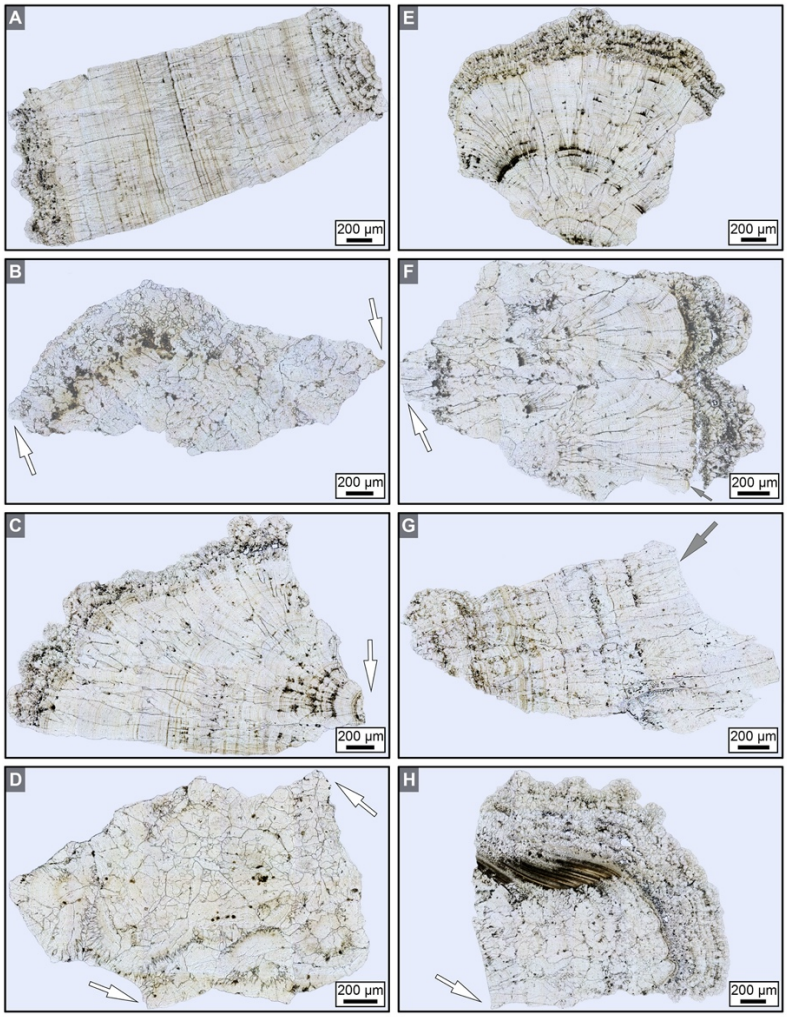

Figure 10. Geometries of ESWL-derived particles from groups 106F2-S1 and 106F4-S1 (Fig. 8). These detailed crystal growth structures and fracture patterns, observed in thin section, are analogous to those observed on the polished epoxy plugs (Figs. 6, 14). The background has been removed from around, but not within each fragment, and replaced with a grey background. (**A**-**H**) BF images showing ESWL fracture geometries that crosscut the original CaOx crystalline architecture. ESWL shock fractures propagate at perpendicular and oblique angles with respect to the original crystalline architecture, often converging to form angles of 60-120^{o} (**B**, **C**, **D**, **F**, **H**, white arrows). Spalling along concentric crystalline layering is also observed (**F**, **G**, grey arrows). ESWL-derived particle locations shown in Figure 8C, F and 9, and complementary CAF and POL figures presented in Figure 11 and 12.

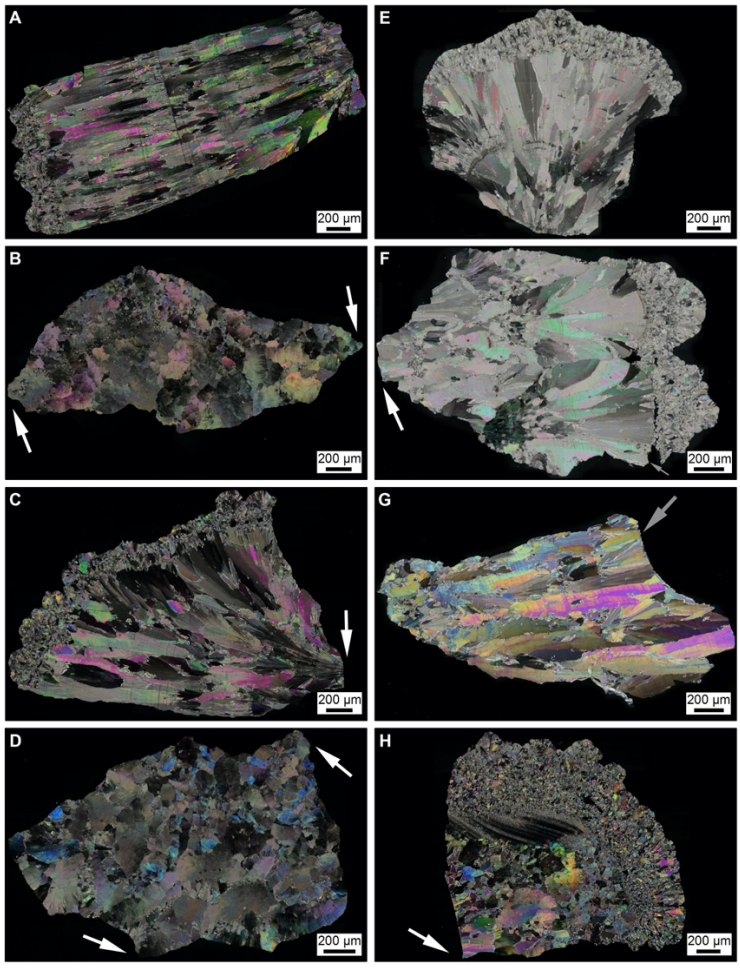

Figure 11. Geometries of ESWL-derived particles from groups 106F2-S1 and 106F4-S1 (Fig. 8). These detailed crystal growth structures and fracture patterns, observed in thin section, are analogous to those observed on the polished epoxy plugs (Figs. 6, 14). The background has been removed from around, but not within each fragment, and replaced with a black background. (**A-H**) POL images showing ESWL fracture geometries that crosscut the original CaOx crystalline architecture. ESWL shock fractures propagate at perpendicular and oblique angles with respect to the original crystalline architecture, often converging to form angles of 60-120º (**B**, **C**, **D**, **F**, **H**, white arrows). Spalling along concentric crystalline layering is also observed (**F**, **G**, grey arrows). ESWL-derived particle locations shown in Figures 8C, F and 9, and complementary CAF and BF figures presented in Figures 10 and 12.

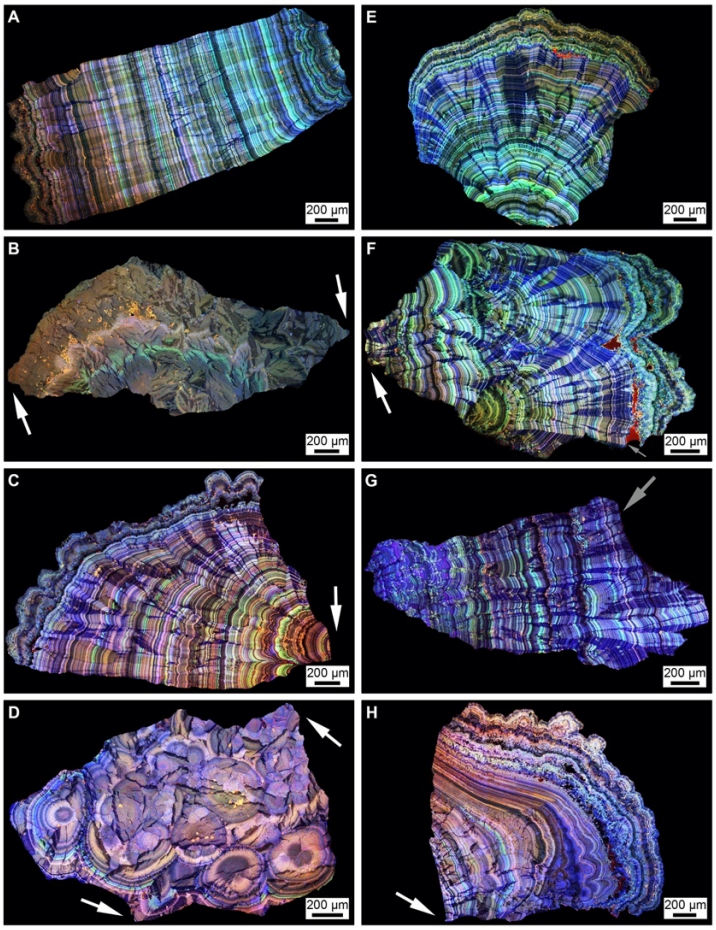

Figure 12. Geometries of ESWL-derived particles from groups 106F2-S1 and 106F4-S1 (Fig. 8). These detailed crystal growth structures and fracture patterns, observed in thin section, are analogous to those observed on the polished epoxy plugs (Figs. 6, 14). Red AF emitted from embedding epoxy has been removed from around, but not within each fragment, and replaced with a black background. (**A**-**H**) CAF images of merged pseudo-colored RGB channels showing ESWL fracture geometries that crosscut the original CaOx crystalline architecture. ESWL shock fractures propagate at perpendicular and oblique angles with respect to the original crystalline architecture, often converging to form angles of 60-120º (**B**, **C**, **D**, **F**, **H**, white arrows). Spalling along concentric crystalline layering is also observed (**F**, **G**, grey arrows). ESWL-derived particle locations shown in Figures 8C, F and 9, and complementary BF and POL figures presented in Figures 10 and 11.

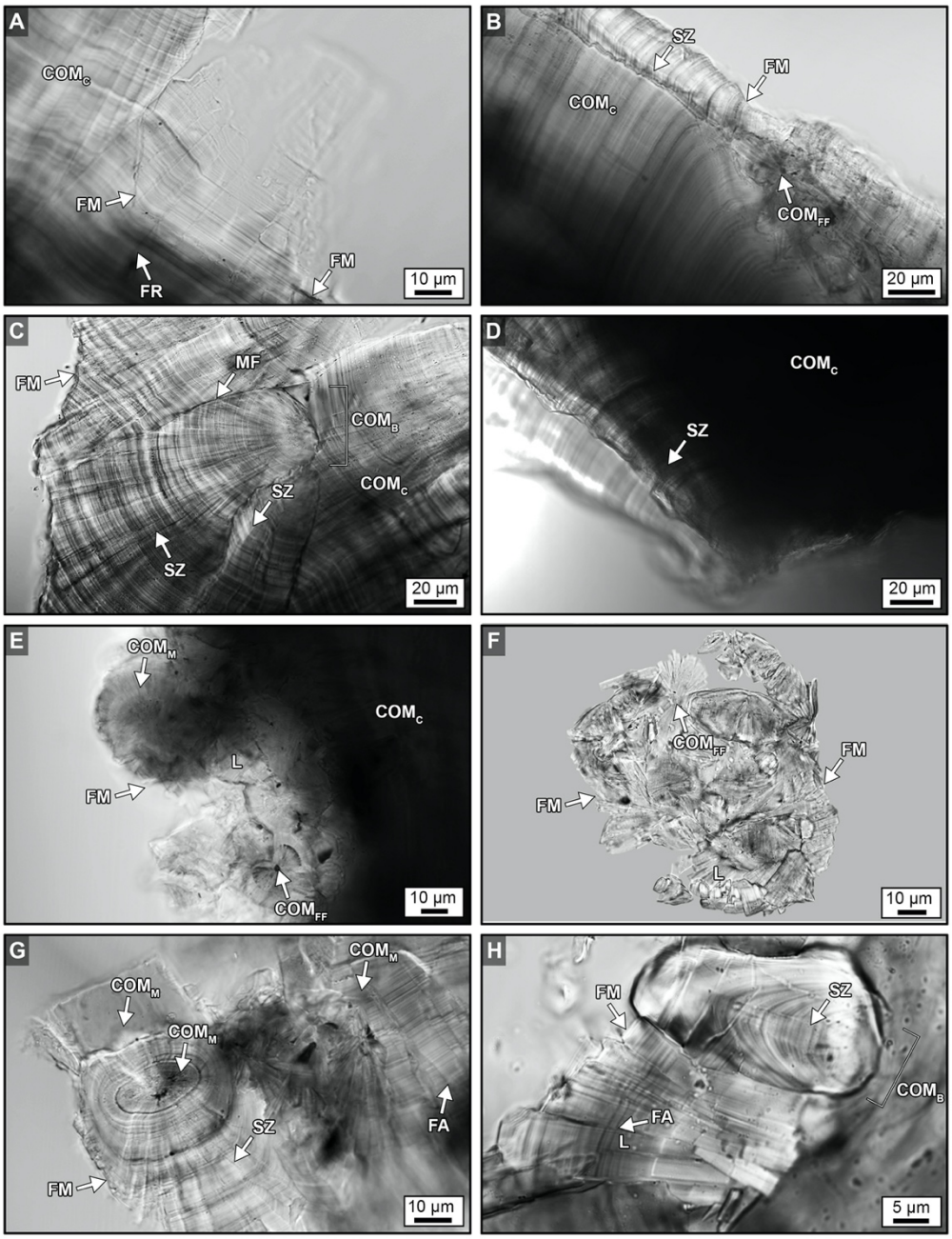

Figure 13. Crystalline architecture and fracture patterns of ESWL-derived particles from groups 106F2-S1 and 106F4-S1 embedded in the epoxy plug shown in Figure 4. (**A**-**H**) T-PMT images. Labels indicate: FR, fracture; FM, fracture margin; FA, fault; L, lath; SZ, sector zone; COM_{FF}, free-floating COM; COM_C, COM cortex; COM_B, bundles of COM radiating from a COM_{FF}; MF, microfractures; COM_M, mimetic replacement COM. Image locations shown in Figure 8C, F and complementary CAF and SRAF figures presented in Figure 14.

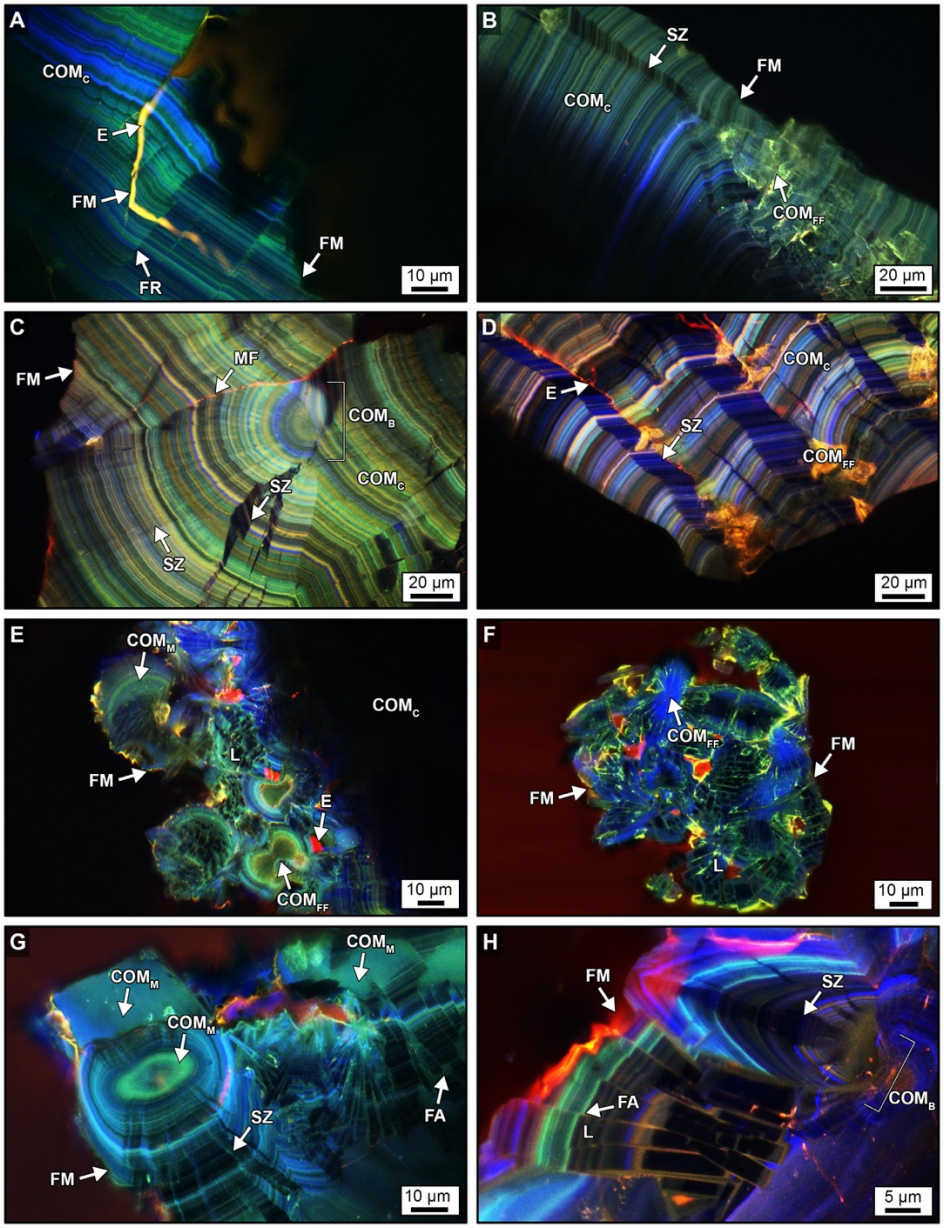

Figure 14. Crystalline architecture and fracture patterns of ESWL-derived particles from groups 106F2-S1 and 106F4-S1 embedded in the epoxy plug shown in Figure 4. (**A**-**G**) CAF images. (**H**) SRAF image. Labels indicate: FR, fracture; FM, fracture margin; FA, fault; L, lath; SZ, sector zone; COM_{FF}, free-floating COM; COM_{C}, COM cortex; COM_{B}, bundles of COM radiating from a COM_{FF}; MF, microfractures; COM_{M}, mimetic replacement COM; and E, red AF embedding epoxy. Image locations shown in Figure 8C, F and complementary T-PMT figure presented in Figure 13.

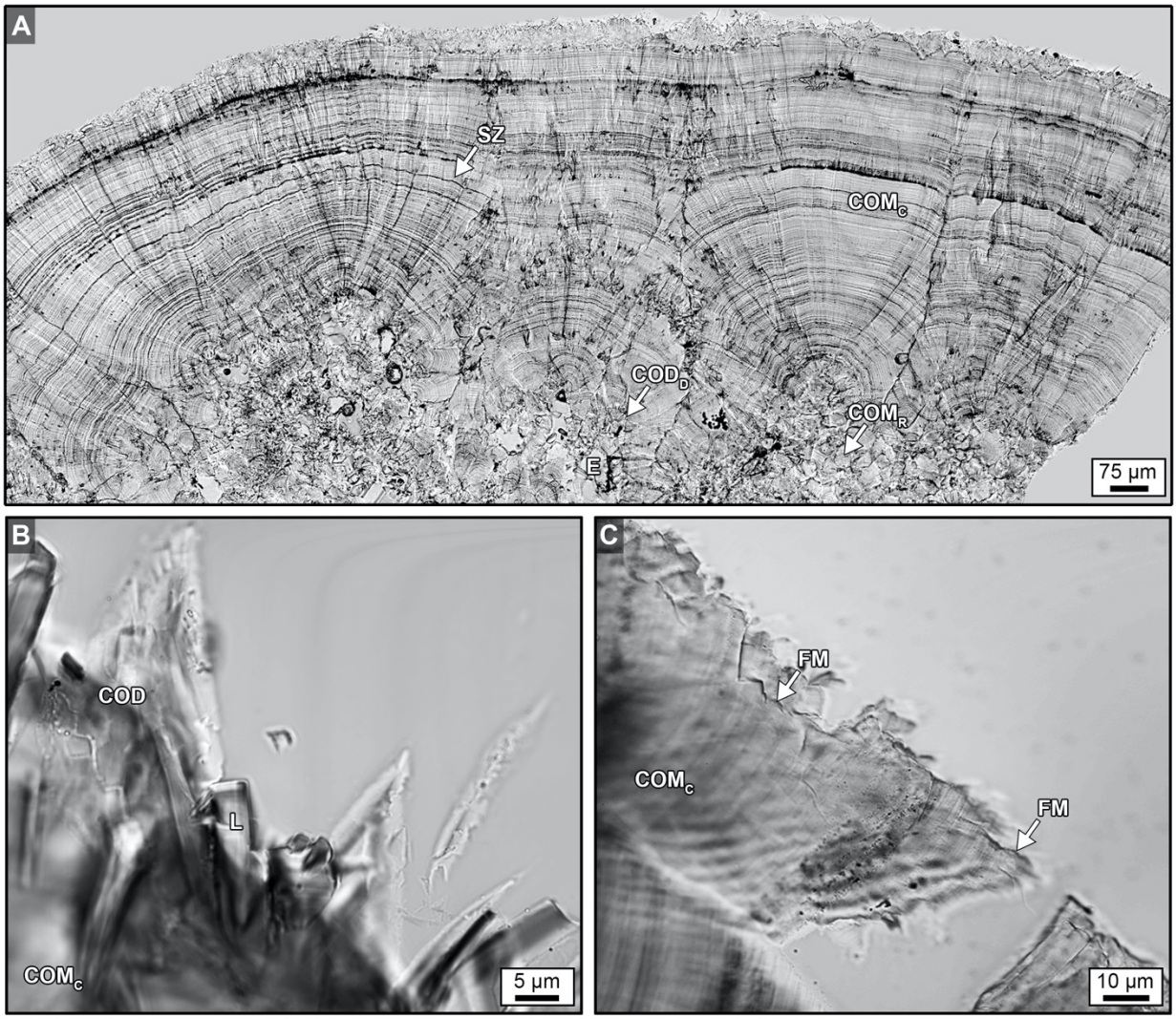

Figure 15. T-PMT images (**A**-**H**) CaOx kidney stone crystalline architecture and fracture patterns. (A) MP2 CaOx kidney stone from Sivaguru et al. (2018). (**B**) Original growth margin containing COD and COM lathes. (**C**) Fracture margins of ESWL-derived particles. Labels indicate: FM, fracture margin; L, lath; SZ, sector zone; COM_C, COM cortex; COM_M, mimetic replacement COM; COD; and COD_D, dissolved COD. Image locations shown in Figure 8C, F and complementary CAF and SRAF figures presented in Figure 16.

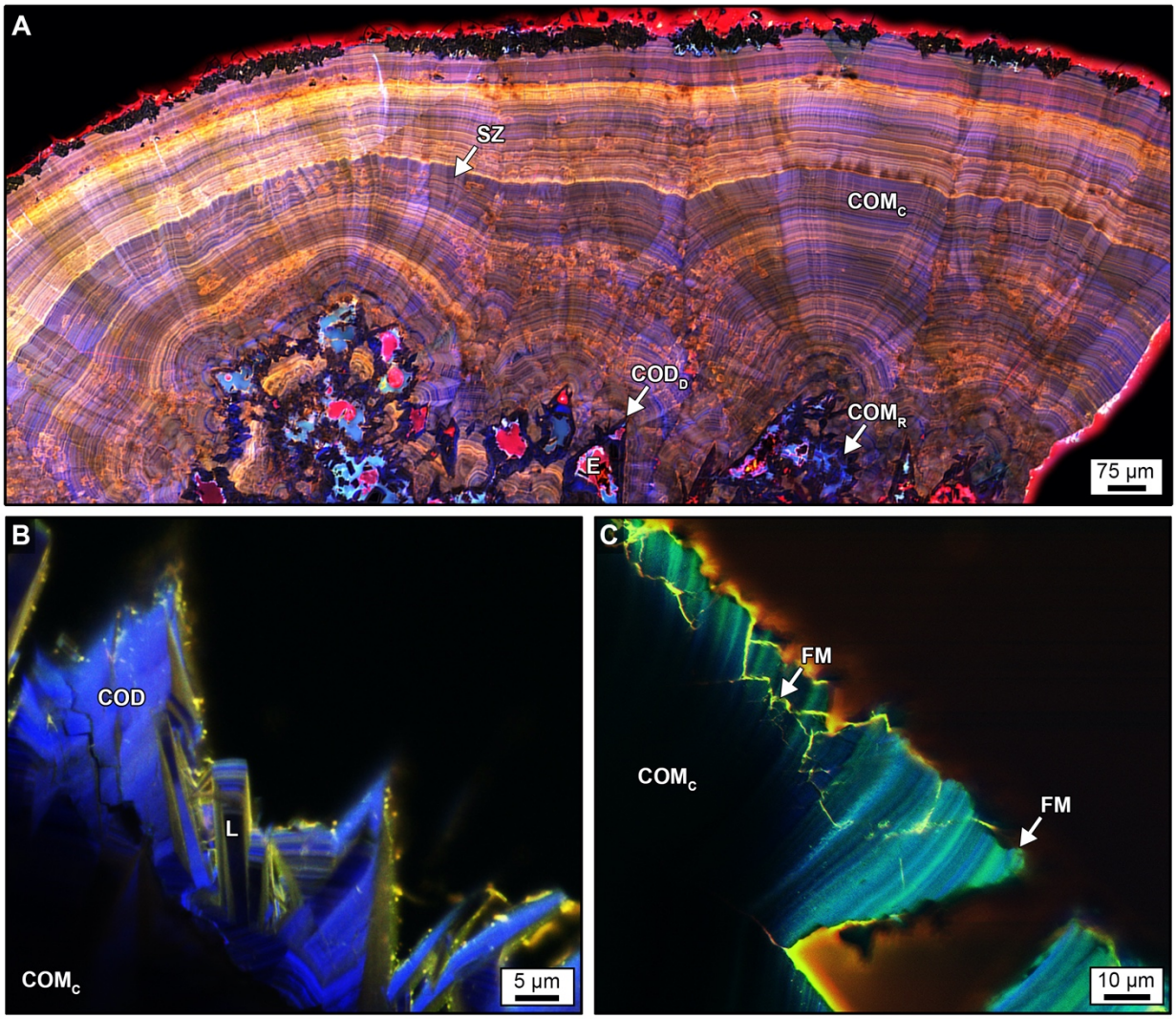

Figure 16. CAF images (**A**, **C**) and SRAF (**B**) images of CaOx kidney stone crystalline architecture and fracture patterns. (A) MP2 CaOx kidney stone from Sivaguru et al. (2018). (**B**) Original growth margin containing COD and COM lathes. (**C**) Fracture margins of ESWL-derived particles. Labels indicate: FM, fracture margin; L, lath; SZ, sector zone; COM_C, COM cortex; COM_M, mimetic replacement COM; COD; and COD_D, dissolved COD. Image locations shown in Figure 8C, F and complementary CAF and SRAF figures presented in Figure 15.

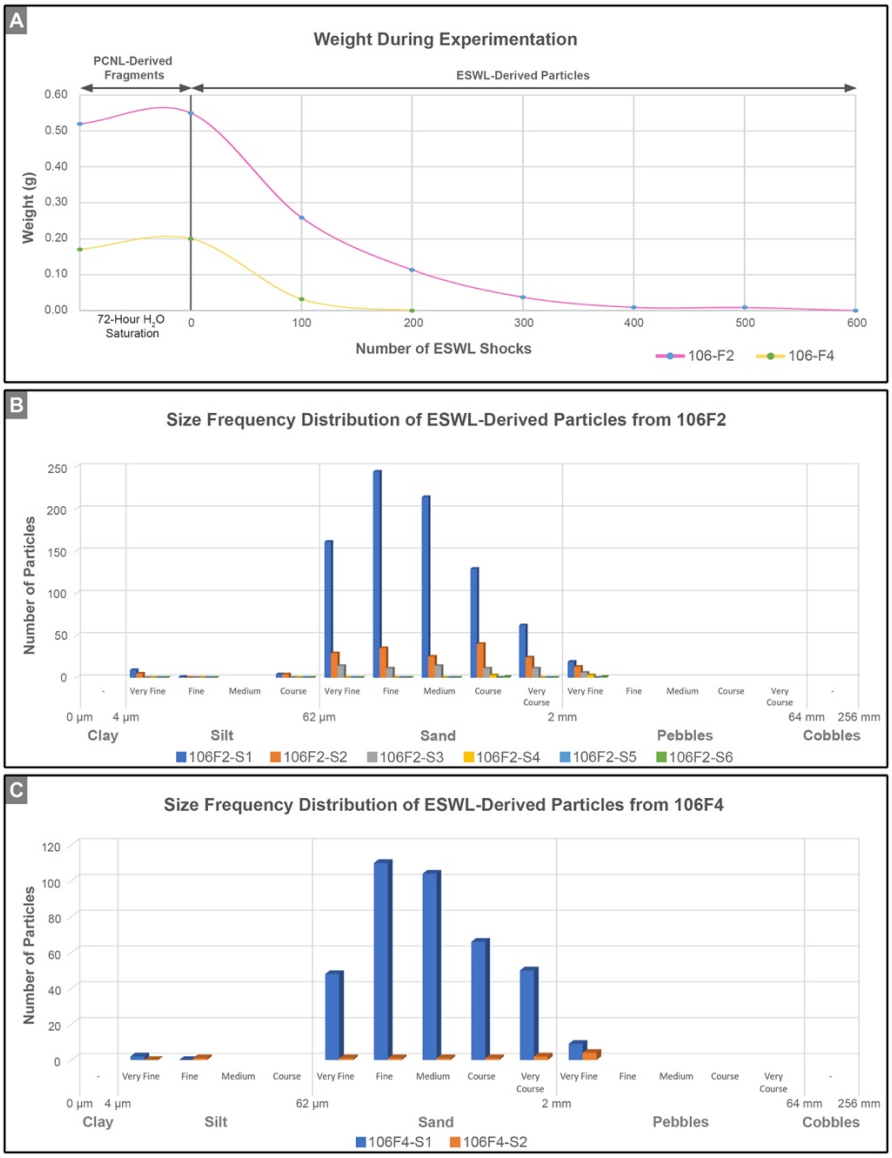

Figure 17. Weight changes and size frequency distributions of ESWL-derived particle groups 106F2 and 106F4. (**A**) Change in weight of PCNL-derived fragments 106F2 and 106F4 after 72-hours of H_2O saturation prior to ESWL experimentation, and weight changes during experimentation in ESWL-derived particles during each incremental 100-shock treatment. Complementary RL images and data are presented in Figure 7 and Table 3. (**B**) Wentworth grain size frequency distribution of ESWL-derived particles from 106F2 after six 100-shock treatments. (**C**) Wentworth grain size frequency distribution of ESWL-derived particles from 106F4 after two 100-shock treatments. Complementary data presented in Table 4.

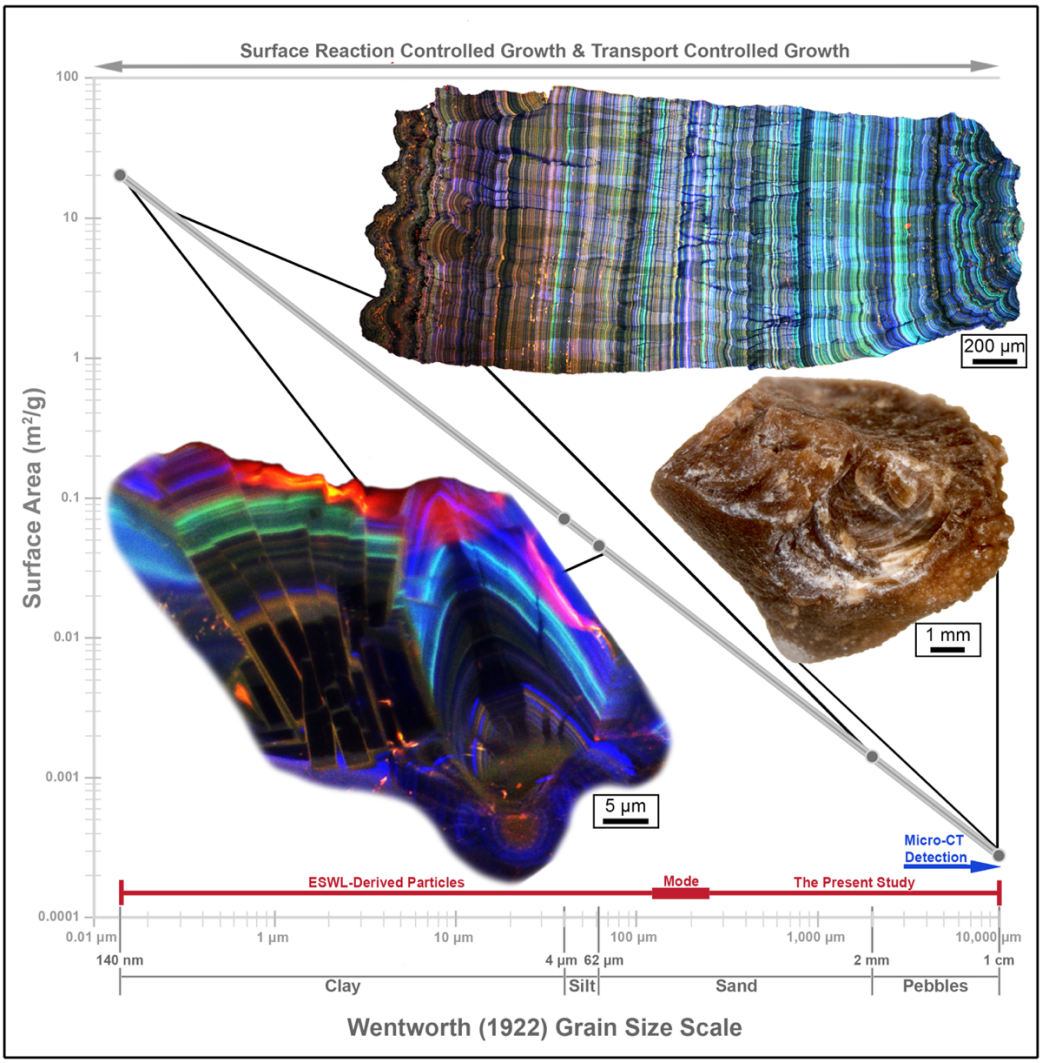

Figure 18. Log plot of specific surface area (m^2/g) as a function of grain diameter (in microns) following the Wentworth grain size classification scheme. Surface area calculations (described in detail in the text) were made from the size frequency distributions of the experimentally measured ESWL-derived particles (Fig. 17; red horizontal line) and assuming geometrically equidimensional particles. The 3-4 mm-diameter detection limit of clinical micro-CT screening (blue line) and example 250 nm-resolution CAF microscopy images are also shown. The 3mm resolution of micro-CT images excludes the high-frequency crystalline architecture and overall ESWL-derived particle fracture geometries. Complementary data found in Supplementary Table 5.

24-Hour Urine Collection Date	Osmolality (mOsm/kg)	pH	SS, CaOx (DG)	SS, Brushite (DG)	SS, Hydroxyapatite (DG)	SS, Uric Acid (DG)	SS, Sodium Urate (DG)
1/16/2012	461	6.2	1.66	-0.60	3.88	-1.54	1.39
4/11/2012	313	5.7	1.31	-0.96	2.25	↑ 1.70	0.21
6/24/2013	364	5.5	↑ 1.92	-2.44	0.43	↑ 2.25	-0.04
6/30/2014	344	5.1	↑ 2.08	-3.67	-1.10	↑ 2.30	-0.71

Table 1. 24-Hour Urine Supersaturation Profile for Patient 106. Acronyms include: SS, supersaturation; and DG, Delta G energy. Arrows indicate above normal concentration range.

24-Hour Urine Collection Date	Na^+ (mmol/ 24 hrs)	K^+ (mmol/ 24 hrs)	Ca^+ (mg/ 24 hrs)	Mg^+ (mg/ 24 hrs)	Cl^- (mmol/ 24 hrs)	PO_4^{3-} (mg/ 24 hrs)	SO_4^{2-} (mmol/ 24 hrs)	Citrate (mg/ 24 hrs)	Oxalate (mmol/ 24 hrs)	Cr (mg/ 24 hrs)
1/16/2012	↑ 423	68	201	115	↑ 441	833	12	↓ 336	↑ 0.59	1173
4/11/2012	-136	43	173	143	113	↑ 1503	16	↓ 363	0.37	1247
6/24/2013	132	↑ 87	102	94	127	↑ 1121	20	354	↑ 0.84	1248
6/30/2014	224	56	172	101	↑ 241	677	20	91	↑ 0.71	883

Table 2. 24-Hour Urine Supersaturation Profile for Patient 106. Abbreviations include: Cr, creatine. Arrows indicate above or below normal concentration range.

Stone	Weight Before H_2O Saturation (g)	Weight After H_2O Saturation(g)	Weight After 100 Shocks (g)	Weigh After 200 Shocks (g)	Weight After 300 Shocks (g)	Weight After 400 Shocks (g)	Weight After 500 Shocks (g)	Weight After 600 Shocks (g)
106-F1	N/A	N/A	N/A	N/A	N/A	N/A	N/A	N/A
106-F2 (ESWL)	0.52	0.55	0.2591	0.1132	0.0373	0.0092	0.0088	0
106-F3	0.56	N/A	N/A	N/A	N/A	N/A	N/A	N/A
106-F4 (ESWL)	0.17	0.20	0.0317	0	N/A	N/A	N/A	N/A

Table 3. Weight of PCNL-derived fragments (106F3, 106F2, and 106F4), change in weight of PCNL-derived fragments 106F2 and 106F4 after 72-hours of H_2O saturation prior to ESWL experimentation, and weight changes during experimentation in ESWL-derived particles during each incremental 100-shock treatment. Complementary RL images and data are presented in Figures 3A, 4, 7, 8, and 17A

Wenworth (1922) Scale	Silt				Sand					Pebbles					Total Fragments
Grain Size Range	(4.01 – 62 µm)				(62 µm – 2 mm)					(2.01 – 64 mm)					
	Very Fine	Fine	Medium	Coarse	Very Fine	Fine	Medium	Coarse	Very Coarse	Very Fine	Fine	Medium	Coarse	Very Coarse	
ESWL-Derived Particles	4.01 - 8.00 µm	8.01 - 16.00 µm	16.01 - 31.00 µm	31.01 - 62.00 µm	62.01 - 125.00 µm	125.01 - 250.00 µm	250.01 - 500.00 µm	500.01 µm - 1.00 mm	1.01 - 2.00 mm	2.01 - 4.00 mm	4.01 - 8.00 mm	8.01 - 16.00 mm	16.01 - 32.00 mm	32.01 - 64.00 mm	
106F2-S1	9	1	0	4	161	244	214	129	62	19	0	0	0	0	843
106F2-S2	5	0	0	4	29	35	25	40	24	13	0	0	0	0	175
106F2-S3	0	0	0	0	14	11	14	11	11	6	0	0	0	0	67
106F2-S4	0	0	0	0	0	0	0	3	0	3	0	0	0	0	6
106F2-S5	0	0	0	0	0	0	0	0	0	0	0	0	0	0	0
106F2-S6	0	0	0	0	0	0	0	1	0	1	0	0	0	0	2
TOTAL	**14**	**1**	**0**	**8**	**204**	**290**	**253**	**184**	**97**	**42**	**0**	**0**	**0**	**0**	**1093**
106F4-S1	2	0	0	0	48	110	104	66	50	9	0	0	0	0	389
106F4-S2	0	1	0	0	1	1	1	1	2	4	0	0	0	0	11
TOTAL	**2**	**1**	**0**	**0**	**49**	**111**	**105**	**67**	**52**	**13**	**0**	**0**	**0**	**0**	**400**

Table 4. Wentworth grain size frequency distribution of ESWL-derived particles from 106F2 and 106F4 after incremental 100-shock ESWL treatments. Complementary data presented in Figure 17B, C.

Grain Size (cm)	1	0.2	0.0064	0.0004	0.000014
Grain Size (µm)	10000	2000	64	4	0.14
Surface Area (m^2/g)	0.000283	0.0014151	0.0442217	0.7075472	20.215633

Table 5. Wentworth grain size surface area calculations. Complementary data to Figure 18.

REFERENCES

Abufaraj, M. X., Tianlin; Cao, Chao; Waldhoer, Thomas; Seitz, Christian; D'andrea, David; Siyam, Abdelmuez; Tarawneh, Rand; Fajkovic, Harun; Schernhammer, Eva; Yang, Lin; Shariat, Shahrokh F. . (2021). Prevalence and Trends in Kidney Stone Among Adults in the USA: Analyses of National Health and Nutrition Examination Survey 2007–2018 Data. *European Urology Focus*, *7*(6), 1468-1475. https://doi.org/10.1016/j.euf.2020.08.011

Barenblatt, G. I. (1962). The Mathematical Theory of Equilibrium Cracks in Brittle Fracture. In (pp. 55-129). Elsevier. https://doi.org/10.1016/s0065-2156(08)70121-2

Berner, R. A. (1980). *Early Diagenesis: A Theoretical Approach*. Princeton University Press.

Bilgren, C. K., Alena; Krause, Rolf; Weinberg, Kerstin. (2018). A phase-field approach to conchoidal fracture

. *Meccanica*, *53*, 1203-1219. https://doi.org/https://doi.org/10.1007/s11012-017-0740-z

Brain, E., Geraghty, R. M., Lovegrove, C. E., Yang, B., & Somani, B. K. (2021). Natural History of Post-Treatment Kidney Stone Fragments: A Systematic Review and Meta-Analysis. *Journal of Urology*, *206*(3), 526-538. https://doi.org/10.1097/ju.0000000000001836

Chaudhri, M. M. (2015). Dynamic fracture of inorganic glasses by hard spherical and conical projectiles. *Philosophical Transactions of the Royal Society A: Mathematical, Physical and Engineering Sciences*, *373*(2038), 20140135. https://doi.org/10.1098/rsta.2014.0135

Chongruksut, W. L., Bannakij; Tawichasri, Chamaiporn; Paichitvichean, Somboon; Euathrongchit, Jantima; Ayudhya, Vorvat Choomsai Na; Patumanond, Jayanton. (2012). Predictors for kidney stones recurrence following extracorporeal shock wave lithotripsy (ESWL) or percutaneous nephrolithotomy (PCNL). *Journal of the Medical Association of Thailand*, *95*(3), 342-348.

Costa-Bauzá, A., Perelló, J., Isern, B., & Grases, F. (2005). An Experimental Study on Residual Lithiasis after Shock Wave Lithotripsy. *Urological Research*, *33*(1), 51-56. https://doi.org/10.1007/s00240-004-0443-5

Costa-Bauzá, A., Perelló, J., Isern, B., Sanchis, P., & Grases, F. (2006). Factors affecting calcium oxalate dihydrate fragmented calculi regrowth. *BMC Urology*, *6*(1). https://doi.org/10.1186/1471-2490-6-16

Dawson, C. H., & Tomson, C. R. (2012). Kidney stone disease: pathophysiology, investigation and medical treatment. *Clinical Medicine*, *12*(5), 467-471. https://doi.org/10.7861/clinmedicine.12-5-467

Dincel, N., Resorlu, B., Unsal, A., Tepeler, A., Silay, M. S., Armagan, A., Diri, A., Sancaktutar, A. A., Ziypak, T., & Mir, S. (2013). Are small residual stone fragments really insignificant in children? *J Pediatr Surg*, *48*(4), 840-844. https://doi.org/10.1016/j.jpedsurg.2012.07.061

Dowty, E. (1976). Crystal structure and crystal growth: II. sector zoning in minerals. *American Mineralogist*, *61*, 460-469.

Du, L. Y. U., Joseph; Nikolov, Hristo N.; Pollmann, Steven I.; Lee, Ting-Yim; Holdsworth, David W. . (2007). A quality assurance phantom for the performanceevaluation of volumetric micro-CT systems. *Physics and Enginnering in Medicine and Biology*, *52*(23), 7087. https://doi.org/10.1088/0031-9155/52

Duan, X., Qu, M., Wang, J., Trevathan, J., Vrtiska, T., Williams, J. C., Krambeck, A., Lieske, J., & McCollough, C. (2013). Differentiation of Calcium Oxalate Monohydrate and Calcium

Oxalate Dihydrate Stones Using Quantitative Morphological Information from Micro-Computerized and Clinical Computerized Tomography. *Journal of Urology*, *189*(6), 2350-2356. https://doi.org/10.1016/j.juro.2012.11.004

Dugdale, D. S. (1960). Yielding of steel sheets containing slits. *Journal of the Mechanics and Physics of Solids*, *8*(2), 100-104. https://doi.org/10.1016/0022-5096(60)90013-2

Eisenmenger, W. (2001). The Mechanisms of Stone Fragmentation in ESWL. *Ultrasound in Medicine & Biology*, *27*(5), 683-693. https://doi.org/https://doi.org/10.1016/S0301-5629(01)00345-3

El-Assmy, A., Harraz, A. M., Eldemerdash, Y., Elkhamesy, M., El-Nahas, A. R., Elshal, A. M., & Sheir, K. Z. (2016). Does lithotripsy increase stone recurrence? A comparative study between extracorporeal shockwave lithotripsy and non-fragmenting percutaneous nephrolithotomy. *Arab Journal of Urology*, *14*(2), 108-114. https://doi.org/10.1016/j.aju.2016.02.004

Evan, A. P. C., Fredric L.; Connors, Bret A.; Handa, Rajash K.; Lingeman, James E.; Worcester, Elaine M. (2015). Mechanism by which shock wave lithotripsy can promote formation of human calcium phosphate stones. *American Journal of Physiology-Renal Physiology*, *308*(8), F938-F949. https://doi.org/https://doi.org/10.1152/ajprenal.00655.2014

Fialkov, J. M., Hedican, S. P., & Fallon, B. (2000). Reassessing the Efficacy of the Dornier MFL-5000 Lithotroptor *Journal of Urology*, *164*(3 Part 1), 640-643. https://doi.org/10.1016/s0022-5347(05)67270-9

Fouke, B. W., Bhattacharjee, A. S., Fried, G. A., Sivaguru, M., Sanford, R. A., Zhou, L., Alcalde, R. E., Wunch, K., Stephenson, A., Ferrar, J. A., Hernandez, A. G., Wright, C., Fields, C. J., Todorov, L. G., Fouke, K. W., Bailey, C. M., & Werth, C. J. (2022). Sulfate-reducing bacteria streamers and iron sulfides abruptly occlude porosity and increase hydraulic resistance in proppant-filled shale fractures. *AAPG Bulletin*, *106*(1), 179-208. https://doi.org/10.1306/07132120124

Fouke, B. W. S., Mayandi. (2021). Calcium Kidney Stones Naturally Undergo 50% by Volume In Vivo Dissolution and Recrystallization via Universal Biomineralization. *26*(5).

García, M. H. (2008). *Sedimentation engineering : processes, measurements, modeling, and practice* American Society of Civil Engineers.

Giannossi, M. L., & Summa, V. (2010). Post-ESWL fragments as core of new kidney stones. *Clinical Kidney Journal*, *3*(4), 405-406. https://doi.org/10.1093/ndtplus/sfq043

Grover, P. K., Kim, D.-S., & Ryall, R. L. (2002). The Effect of Seed Crystals of Hydroxyapatite and Brushite on the Crystallization of Calcium Oxalate in Undiluted Human Urine In Vitro: Implications for Urinary Stone Pathogenesis. *Molecular Medicine*, *8*(4), 200-209. https://doi.org/10.1007/bf03402012

Hesse, A., Brändle, E., Wilbert, D., Köhrmann, K. U., & Alken, P. (2003). Study on the Prevalence and Incidence of Urolithiasis in Germany Comparing the Years 1979 vs. 2000. *European Urology*, *44*(6), 709-713. https://doi.org/10.1016/s0302-2838(03)00415-9

Hsi, R. S., Sanford, T., Goldfarb, D. S., & Stoller, M. L. (2017). The Role of the 24-Hour Urine Collection in the Prevention of Kidney Stone Recurrence. *Journal of Urology*, *197*(4), 1084-1089. https://doi.org/10.1016/j.juro.2016.10.052

Hyams, E. S. B., Aron; Lipkin, Michael; Shah, Ojas. (2010). Heterogeneity in the Reporting of Disease Characteristics and Treatment Outcomes in Studies Evaluating Treatments for

Nephrolithiasis. *Journal of Endourology*, *24*(9), 1411-1414. https://doi.org/doi: 10.1089/end.2009.0645.
Kachanov, L. M. (1986). *Introduction to Continuum Damage Mechanics* (Vol. 10). Kluwer.
Kamihira, O., Ono, Y., Katoh, N., Yamada, S., Mizutani, K., & Ohshima, S. (1996). Long-Term Stone Recurrence Rate After Extracorporeal Shock Wave Lithotripsy. *Journal of Urology*, *156*(4), 1267-1271. https://doi.org/10.1016/s0022-5347(01)65566-6
Kang, M., Son, H., Jeong, H., Cho, M. C., & Cho, S. Y. (2016). Clearance rates of residual stone fragments and dusts after endoscopic lithotripsy procedures using a holmium laser: 2-year follow-up results. *World Journal of Urology*, *34*(11), 1591-1597. https://doi.org/10.1007/s00345-016-1807-5
Keeley, J. F. X., Moussa, S. A., Smith, G., & Tolley, D. A. (1999). Clearance of Lower-Pole Stones following Shock Wave Lithotripsy: Effect of the Infundibulopelvic Angle. *European Urology*, *36*(5), 371-375. https://doi.org/10.1159/000020016
Khaitan, A., Gupta, N. P., Hemal, A. K., Dogra, P. N., Seth, A., & Aron, M. (2002). Post-ESWL, clinically insignificant residual stones: reality or myth? *Urology*, *59*(1), 20-24. https://doi.org/10.1016/s0090-4295(01)01494-7
Khan, S. R., Pearle, M. S., Robertson, W. G., Gambaro, G., Canales, B. K., Doizi, S., Traxer, O., & Tiselius, H.-G. (2016). Kidney stones. *Nature Reviews Disease Primers*, *2*(1), 16008. https://doi.org/10.1038/nrdp.2016.8
Khan, S. R. H., Raymond L.; Finlayson, Birdwell. (1986). Morphology of Urinary Stone Particles Resulting from ESWL Treatment. *The Journal of Urology*, *136*(6), 1367-1372. https://doi.org/https://doi.org/10.1016/S0022-5347(17)45340-7
Köhrmann, K. U., Rassweiler, J., & Alken, P. (1993). The recurrence rate of stones following ESWL. *World Journal of Urology*, *11*(1). https://doi.org/10.1007/bf00182167
Lasaga, A. C. K., R. J.; Berner, R. A.; Fisher, G. W.; Anderson, D. E. (1981). *Kinetics of Geochemical Processes* (Vol. 8). De Gruyter. https://doi.org/doi: 10.1515/9781501508233
Lautz, J., Sankin, G., & Zhong, P. (2013). Turbulent water coupling in shock wave lithotripsy. *Physics in Medicine and Biology*, *58*(735). https://doi.org/10.1088/0031-9155/58
Li, X. H., Long; Li, Jianzhong; Duan, Zhongyang; Gao, Zijian; Liu, Long. (2015). Medium-term follow-up of clinically insignificant residual fragments after minimal invasive percutaneous nephrolithotomy: prognostic features and risk factors. *International Journal of Clinical and Experimental Medicine*, *8*(11).
Liu, Y., & Zhong, P. (2002). BegoStone—a new stone phantom for shock wave lithotripsy research (L). *The Journal of the Acoustical Society of America*, *112*(4), 1265-1268. https://doi.org/10.1121/1.1501905
Lokhandwalla, M., & Sturtevant, B. (2000). Fracture mechanics model of stone comminution in ESWL and implications for tissue damage. *Physics in Medicine and Biology*, *45*(7), 1923-1940. https://doi.org/10.1088/0031-9155/45/7/316
McAteer, J. A., & Evan, A. P. (2008). The Acute and Long-Term Adverse Effects of Shock Wave Lithotripsy. *Seminars in Nephrology*, *28*(2), 200-213. https://doi.org/10.1016/j.semnephrol.2008.01.003
McAteer, J. A., Williams, J. C., Cleveland, R. O., Van Cauwelaert, J., Bailey, M. R., Lifshitz, D. A., & Evan, A. P. (2005). Ultracal-30 gypsum artificial stones for research on the mechanisms of stone breakage in shock wave lithotripsy. *Urological Research*, *33*(6), 429-434. https://doi.org/10.1007/s00240-005-0503-5

McLean, R. J. C., & Nickel, J. C. (1994). Glycosaminoglycans and struvite calculi. *World Journal of Urology*, *12*(1). https://doi.org/10.1007/bf00182051
Micali, S., Sighinolfi, M. C., Celia, A., De Stefani, S., Grande, M., Cicero, A. F., & Bianchi, G. (2006). Can Phyllanthus niruri Affect the Efficacy of Extracorporeal Shock Wave Lithotripsy for Renal Stones? A Randomized, Prospective, Long-Term Study. *Journal of Urology*, *176*(3), 1020-1022. https://doi.org/10.1016/j.juro.2006.04.010
Miller, N. L., & Lingeman, J. E. (2007). Management of kidney stones. *BMJ*, *334*(7591), 468-472. https://doi.org/10.1136/bmj.39113.480185.80
Moon, Y. T., Kim, Sae Chul. (1993). Fate of Clinically Insignificant Residual Fragments after Extracorporeal Shock Wave Lithotripsy with EDAP LT-01 Lithotripter. *Journal of Endourology*, *7*(6), 453-456. https://doi.org/10.1089/end.1993.7.453
Mota, A. K., Jaroslaw; Ortiz, Michael. (2006). Three-dimensional fracture and fragmentation of artifical kidney stones. *Journal of Physics: Conference Series*, *46*, 299-303. https://doi.org/10.1088/1742-6596/46
Najeeb, Q. M., Imran; Bhaskar, Neeru; Kaur, Harnam; Singh, Jasbir; Pandey, Rajesh; Sodhi, KS; Prasad, Suvarna; Ishaq, Sheikh; Mahajan, Ruhi. (2013). *Saudi Journal of Kidney Diseases and Transpantation 24*(1), 60-66. https://doi.org/10.4103/1319-2442.106243
Osman, M. M., Alfano, Y., Kamp, S., Haecker, A., Alken, P., Michel, M. S., & Knoll, T. (2005). 5-year-follow-up of Patients with Clinically Insignificant Residual Fragments after Extracorporeal Shockwave Lithotripsy. *European Urology*, *47*(6), 860-864. https://doi.org/10.1016/j.eururo.2005.01.005
Penniston, K. L., McLaren, I. D., Greenlee, R. T., & Nakada, S. Y. (2011). Urolithiasis in a Rural Wisconsin Population From 1992 to 2008: Narrowing of the Male-to-Female Ratio. *Journal of Urology*, *185*(5), 1731-1736. https://doi.org/10.1016/j.juro.2010.12.034
Pfau, A., & Knauf, F. (2016). Update on Nephrolithiasis: Core Curriculum 2016. *American Journal of Kidney Diseases*, *68*(6), 973-985. https://doi.org/10.1053/j.ajkd.2016.05.016
Pishchalnikov, Y. A., McAteer, J. A., Williams, J. C., Pishchalnikova, I. V., & Vonderhaar, R. J. (2006). Why Stones Break Better at Slow Shockwave Rates Than at Fast Rates: In Vitro Study with a Research Electrohydraulic Lithotripter. *Journal of Endourology*, *20*(8), 537-541. https://doi.org/10.1089/end.2006.20.537
Pittomvils, G. V., H.; Wevers, M.; Lagaut, J.P.; De Ridder, D.; De Meester, P.; Boving, R; Baert, L. (1994). The influence of internal stone structure upon the fracture behavior of urinary calculi. *Ultrasound in Medicine & Biology*, *20*(8), 803-810. https://doi.org/https://doi.org/10.1016/0301-5629(94)90037-X
Qin, J., Simmons, W. N., Sankin, G., & Zhong, P. (2010). Effect of lithotripter focal width on stone comminution in shock wave lithotripsy. *The Journal of the Acoustical Society of America*, *127*(4), 2635-2645. https://doi.org/10.1121/1.3308409
Rassweiler, J. J., Knoll, T., Köhrmann, K.-U., McAteer, J. A., Lingeman, J. E., Cleveland, R. O., Bailey, M. R., & Chaussy, C. (2011). Shock Wave Technology and Application: An Update. *European Urology*, *59*(5), 784-796. https://doi.org/10.1016/j.eururo.2011.02.033
Reihle Jr., R. A. C., H. Ballantine; Vaughan Jr., E. D. (1987). Quantitative and Crystallographic Analysis of Stone Fragments Voided After Extracorporeal Shock Wave Lithotripsy. *Journal of Endourology*, *1*(1), 37-44. https://doi.org/https://doi.org/10.1089/end.1987.1.37
Roberts, S. D., & Resnick, M. I. (1986). Glycosaminoglycans Content of Stone Matrix. *Journal of Urology*, *135*(5), 1078-1083. https://doi.org/10.1016/s0022-5347(17)45979-9

Sabnis, R. B., Naik, K., Desai, M. R., Bapat, S.D. (1997). Extracorporeal shock wave lithotripsy for lower calyceal stones: Can clearance be pre-dicted? . *British Journal of Urology*, *80*(6), 853-857. https://doi.org/10.1046/j.1464-410x.1997.00436.x

Sapozhnikov, O. A., Maxwell, A. D., Macconaghy, B., & Bailey, M. R. (2007). A mechanistic analysis of stone fracture in lithotripsy. *The Journal of the Acoustical Society of America*, *121*(2), 1190-1202. https://doi.org/10.1121/1.2404894

Sass, W. B., Martin; Dreyer, Hans-Peter; Matura, Eike; Folberth, Walter, Preismeyer, Hans-Georg; Seifert, Jürgen. (1991). The mechanisms of stone disintegration by shock waves *Ultrasound in Medicine & Biology*, *17*(3), 239-243. https://doi.org/https://doi.org/10.1016/0301-5629(91)90045-X

Saw, J. J., Sivaguru, M., Wilson, E. M., Dong, Y., Sanford, R. A., Fields, C. J., Cregger, M. A., Merkel, A. C., Bruce, W. J., Weber, J. R., Lieske, J. C., Krambeck, A. E., Rivera, M. E., Large, T., Lange, D., Bhattacharjee, A. S., Romero, M. F., Chia, N., & Fouke, B. W. (2021). In Vivo Entombment of Bacteria and Fungi during Calcium Oxalate, Brushite, and Struvite Urolithiasis. *Kidney360*, *2*(2), 298-311. https://doi.org/10.34067/kid.0006942020

Scales, C. D., Smith, A. C., Hanley, J. M., & Saigal, C. S. (2012). Prevalence of Kidney Stones in the United States. *European Urology*, *62*(1), 160-165. https://doi.org/10.1016/j.eururo.2012.03.052

Shigeta, M., Kasaoka, Y., Yasumoto, H., Inoue, K., Usui, T., Hayashi, M., & Tazuma, S. (1999). Fate of residual fragments after successful extracorporeal shock wave lithotripsy. *International Journal of Urology*, *6*(4), 169-172. https://doi.org/10.1046/j.1442-2042.1999.06443.x

Sivaguru, M., Lieske, J. C., Krambeck, A. E., & Fouke, B. W. (2020). GeoBioMed sheds new light on human kidney stone crystallization and dissolution. *Nature Reviews Urology*, *17*(1), 1-2. https://doi.org/10.1038/s41585-019-0256-5

Sivaguru, M., Saw, J. J., Williams, J. C., Lieske, J. C., Krambeck, A. E., Romero, M. F., Chia, N., Schwaderer, A. L., Alcalde, R. E., Bruce, W. J., Wildman, D. E., Fried, G. A., Werth, C. J., Reeder, R. J., Yau, P. M., Sanford, R. A., & Fouke, B. W. (2018). Geobiology reveals how human kidney stones dissolve in vivo. *Scientific Reports*, *8*(1). https://doi.org/10.1038/s41598-018-31890-9

Sivaguru, M., Saw, J. J., Wilson, E. M., Lieske, J. C., Krambeck, A. E., Williams, J. C., Romero, M. F., Fouke, K. W., Curtis, M. W., Kear-Scott, J. L., Chia, N., & Fouke, B. W. (2021). Human kidney stones: a natural record of universal biomineralization. *Nature Reviews Urology*. https://doi.org/10.1038/s41585-021-00469-x

Smith, N., & Zhong, P. (2012). Stone comminution correlates with the average peak pressure incident on a stone during shock wave lithotripsy. *Journal of Biomechanics*, *45*(15), 2520-2525. https://doi.org/10.1016/j.jbiomech.2012.07.025

Stamatelou, K. K. F., Mildred E.; Jones, Camille A.; Nyberg, Leroy M.; Curhan, Gary C. (2003). Time trends in reported prevalence of kidney stones in the United States: 1976-1994. *Kidney International*, *63*(5). https://doi.org/10.1046/j.1523-1755.2003.00917.x

Streem, S. B., Yost, A., & Mascha, E. (1996). Clinical Implications of Clinically Insignificant Stone Fragments After Extracorporeal Shock Wave Lithotripsy. *Journal of Urology*, *155*(4), 1186-1190. https://doi.org/10.1016/s0022-5347(01)66208-6

Sun, B. Y.-C., Lee, Y.-H., Jiaan, B.-P., Chen, K.-K., Chang, L. S., & Chen, K.-T. (1996). Recurrence rate and risk factors for urinary calculi after extracorporeal shock wave

lithotripsy. *Journal of Urology*, *156*(3), 903-906. https://doi.org/10.1016/s0022-5347(01)65657-x

Tan, Y. H., & Wong, M. (2005). How Significant are Clinically Insignificant Residual Fragments Following Lithotripsy? *Current Opinion in Urology*, *15*(2), 127-131. https://doi.org/doi: 10.1097/01.mou.0000160628.43860.f9

Tang, R., Nancollas, G. H., Giocondi, J. L., Hoyer, J. R., & Orme, C. A. (2006). Dual roles of brushite crystals in calcium oxalate crystallization provide physicochemical mechanisms underlying renal stone formation. *Kidney International*, *70*(1), 71-78. https://doi.org/10.1038/sj.ki.5000424

Thongprayoon, C., Krambeck, A. E., & Rule, A. D. (2020). Determining the true burden of kidney stone disease. *Nature Reviews Nephrology*, *16*(12), 736-746. https://doi.org/10.1038/s41581-020-0320-7

Trinchieri, A., Coppi, F., Montanari, E., Del Nero, A., Zanetti, G., & Pisani, E. (2000). Increase in the Prevalence of Symptomatic Upper Urinary Tract Stones during the Last Ten Years. *European Urology*, *37*(1), 23-25. https://doi.org/10.1159/000020094

Uribarri, J. O., Man S.; Carroll, Hugh J. . (1989). The First Kidney Stone. *Annals of Internal Medicine*, *111*(12), 1006-1009. https://doi.org/https://doi.org/10.7326/0003-4819-111-12-1006

Urological Diseases in America. (2012). (Chapter 9: Urinary Tract Stones Issue. U. S. G. P. Office.

Villarroel, M. A. B., D. L.; Jen, A. (2019). *Tables of Summary Health Statistics for U.S. Adults: 2018 National Health Interview Survey*. http://www.cdc.gov/nchs/nhis/SHS/tables.htm.

Walter, L. M. M., John W. . (1984). Reactive Surface Area of Skeletal Carbonates During Dissolution: Effect of Grain Size. *SEPM Journal of Sedimentary Research*, *Vol. 54*. https://doi.org/10.1306/212f8562-2b24-11d7-8648000102c1865d

Wentworth, C. K. (1922). A Scale of Grade and Class Terms for Clastic Sediments. *The Journal of Geology*, *30*(5), 377-392. https://doi.org/10.2307/30063207

Wess, O. J., & Mayer, J. (2020). Fragmentation of brittle material by shock wave lithotripsy. Momentum transfer and inertia: a novel view on fragmentation mechanisms. *Urolithiasis*, *48*(2), 137-149. https://doi.org/10.1007/s00240-018-1102-6

Zanetti, G., Seveso, M., Montanari, E., Guarneri, A., Del Nero, A., Nespoli, R., & Trinchieri, A. (1997). Renal Stone Fragments Following Shock Wave Lithotripsy. *Journal of Urology*, *158*(2), 352-355. https://doi.org/10.1016/s0022-5347(01)64476-8

Zhong, P. (2013). *Bubble Dynamics and Shock Waves*. Springer-Verlag.

Zisman, A. L. (2017). Effectiveness of Treatment Modalities on Kidney Stone Recurrence. *Clinical Journal of the American Society of Nephrology*, *12*(10), 1699-1708. https://doi.org/10.2215/cjn.11201016

APPENDIX A
SUPPLMENTARY MATERIALS & METHODS

PERMITS, IRB APPROVAL, AND PATIENT CONSENT

This basic medical research study was reviewed and approved by the Institutional Review Board (IRB 09-002083) at the Mayo Clinic, and the outcomes of this study will positively affect the future management of kidney stone treatment. The patient provided written informed consent. Preoperative data was collected consisting of the patient age, sex, BMI, prior surgical history, prior metabolic stone therapies, stone location based on micro-CT scan (3mm resolution), and stone density measurement (hounsfield units). Approximately, 3-6 months after stone removal, the patient completed a metabolic evaluation for stone disease, which included 24-hour urine collection for supersaturation profile (EQUIL2). Medical history, standard serum labs, medication intake (e.g. citrate, thiazides, allopurinol), and comorbid conditions (e.g. diabetes mellitus, obesity, gout, hypertension, distal rental tubular acidosis, malabsorption-related conditions and diseases) were assessed from the medical record.

PATIENT METADATA COLLECTION

One patient was selected for this study who formed a kidney stone primarily composed of calcium oxalate monohydrate (COM). Patient 106 was a 60-year-old female diagnosed with an episode of gross hematuria and urinary tract infection in late 2011. In 2005, the patient was status post Roux-en-Y gastric bypass for hypertension and obesity. Previous medical and surgical history of the patient includes hysterectomy for fibroids and endometriosis, degenerative joint disease, hypothyroidism, posttraumatic stress disorder, multiple personality disorder, depression, post-cholecystectomy syndrome, bladder repair for incontinence, C-section during childbirth, type 2

diabetes mellitus, abnormal adenosine sestamibi (February 2020) with a small reversible apical defect, and a laparoscopic gastric bypass (November 2005). After the gastric bypass procedure, they lost ~120lbs, although they gained 70Lbs in the following years. The patient indicated symptoms of loose stools post-surgery, especially when eating foods with higher fat content. When the patient followed a proper diet, their daily bowl movements were more consistent. The patient had one stone (1.8cm x 1.1cm) found in the left renal pelvis and one stone (8mm) with likely more smaller stones found in the left lower pole. The patient underwent percutaneous nephrolithotomy (PCNL) on February 28, 2012, and March 1, 2012, followed by the removal of some stone fragments on March 11, 2012. The left ureteral stent was removed on March 12, 2012. Follow-up CT results indicated no residual stones. The patient has been asymptomatic since the procedure with no further kidney stone issues.

URINE COLLECTION, PCNL PROCEDURE, AND KIDNEY STONE RETRIEVAL

One month prior to the PCNL intervention, the patient was required to submit a 24-hour urine collection sample on January 16, 2012. Stones were removed during surgery using standard PCNL procedures (Patil, 2010, Sivaguru et al., 2018) conditions by A. E. Krambeck (author) within a sterile operating room at the Mayo Clinic in Rochester, Minnesota. The procedure began by an anesthesiologist administering pre-incision antibiotics and inducing anesthesia to the patient on a stretcher. Subsequently, a 100mL of catheterized urine sample was sterilely obtained and placed into DNA/RNAse free specimen cup by a member of the urology research team. The urine was filtered through a 0.22μm filter into three 15mL DNA/RNAse free Falcon tubes and 50mL DNA/RNAse Falcon tubes. These samples were placed in a -80°C storage freezer within 1 hour. Subsequently, Patient 106 was properly positioned and draped on the operating room (OR) table

for the surgical procedure under sterile operating room conditions. The urologist obtained percutaneous access into the kidney using fluoroscopic guidance, while the urology research team obtained fluoroscopic images for 3D contextual information of the stone location prior to shock pulse lithotripsy (SPL). The kidney stones were dislodged and fragmented by the SPL probe, collected, and sent for culturing. The PCNL-derived fragments were immediately placed in a DNA/RNAse free sample cup to be stored at -80°C storage freezer within 1 hour. The patient was subsequently required to submit 24-hour urine collections one month (April 11, 2012), one year (June 24, 2013), and two years (June 30, 2014) post-PCNL intervention. The frozen urine and stone fragments were transported to the University of Illinois at Urbana-Champaign (Illinois) at -80°C Taylor-Wharton CX Series dry shipper dewar (Borehamwood, UK), and shipped to the BSL2-certified geobiology laboratory in the Carl R. Woese Institute for Genomic Biology (IGB) at Illinois. The Mayo Clinic also provided the Fouke laboratory with detailed chemical composition of the four 24-hour urine samples.

PCNL-DERIVED KIDNEY STONE FRAGMENT INITIAL IMAGING

PCNL-derived kidney stone fragments 106F1-4 and urine samples from Patient 106 were thawed for 24 hours and dried for an additional 24 hours at room temperature. All four kidney stone fragments (106F1-4) were imaged using reflective microscopy on the Zeiss Axio Zoom.V16 microscope with a 1.0x Plan-NeoFluar Z (0.25 NA) objective, Axiocam 512 color camera, and a 1x Camera Adapter at a 7-8.2x total magnification (Carl Zeiss, Oberkochen, Germany; Figs. 3A, 4). The objective, camera, and camera adapter were consistently used for subsequent Zeiss Axio Zoom.V16 imaging in this study, unless otherwise noted.

X-ray images at 3µm-resolution were also collected on all samples using the micro computed tomography (micro-CT) on the North Star Imaging X3000 Industrial 3D X-Ray Inspection system. PCNL-derived fragment was scanned with the following parameters: voltage of 90kV, current of 40µA, focal spot size 3.6µm, focal spot mode microfocus, 10 frames per second, detector pixel pitch of 0.0635mm x 0.0635mm, horizontal flip, 180° rotation, tube to object distance of 12.801mm, tube to detection distance of 220.001mm, zoom factor of 16.43x, effective pixel pitch 0.00739mm, 2520 projections, voxel size of 3.9µm, and geometric unsharpness of 15.4x. PCNL-derived fragment 106F2 was scanned with the following parameters: voltage of 90kV, current of 40µA, focal spot size 3.6µm, focal spot mode microfocus, 10 frames per second, detector pixel pitch of 0.0635mm x 0.0635mm, horizontal flip, 180° rotation, tube to object distance of 12.799mm, tube to detection distance of 220.001mm, zoom factor of 16.42x, effective pixel pitch 0.007388mm, 60 projections, voxel size of 3.9µm, and geometric unsharpness of 15.4x. PCNL-derived fragments 106F3 and 106F4 were scanned with the following parameters: voltage of 90kV, current of 40µA, focal spot size 3.6µm, focal spot mode microfocus, 10 frames per second, detector pixel pitch: 0.0635mm x 0.0635mm, horizontal flip, 180° rotation, tube to object distance of 17.729mm, tube to detection distance of 220.76mm, zoom factor of 12.02x, effective pixel pitch 0.01023mm, 2520 projections, voxel size of 5.3µm and geometric unsharpness of 11x. This permitted the generation of several thousand images per core. Raw data images were converted to Tiff files at both 8-bit and 16-bit scales for visualization. The images were resized using NIH Image J Software (https://imagej.nih.gov/ij/).

PCNL-DERIVED STONE FRAGMENT EXPERIMENTAL PREPARATION

PCNL-derived fragment 106F1 was sacrificed for experiment standardization. PCNL-derived fragments 106F2 and 106F4 were initially weighed, then saturated for 72 hours with 24-hour degassed 18.2 MilliQ H_2O within a vacuum chamber (McAnteer, 2005). The samples were then rinsed for 10 minutes in a fresh beaker of 24+ hour degassed 18.2 MilliQ water using forceps to remove any dissociated particles from the stones. The stones were then gently tapped onto a Kim wipe and transferred to a weigh boat to record the final weight prior to the ESWL experiment. The 72-hour-H_2O saturated sample was then used for the ESWL fragmentation experiment within the hour.

DORNIER ESWL INSTRUMENT PREPARATION

The Dornier Delta® III urological workstation instrument (https://www.dornier.com/products/) containing the ESWL was donated by Dornier MedTech to the Fouke Lab at the UIUC and was used for this study. Prior to initiating the experiment, the instrument was warmed up and LithoClear Lithotripsy gel (https://www.coneinstruments.com/lubrication/p/LithoClear-Lithotripsy-Gel/) was strategically mounted on the bellow with limited air bubbles. This was done by holding the gel container at the center of the bellow with little movement to create a large mound, then using a spatula to remove air bubbles and evenly distribute the gel across the top of the bellow.

This study used the provided calibration container for the ESWL fragmentation experiment since it was designed to mimic the tissue-kidney structure with a direct shockwave focal point at the center, 2mm-mesh net containing the sample (Pishchalnikov et al., 2006). The container was attached to the ESWL, and the bellow coupling pressure was shifted from 5 to 4 to properly adhere

the gel onto both the bellow and test container surface. The presence of bubbles within the gel can interfere with the shock penetration. If bubbles were present, the edge of the bellow was pressed downward to move the trapped air out from the gel, or the instrument was left for running to allow the radiating heat to remove any remaining bubbles. Subsequently, 1000mL of 18.2 MilliQ water was poured into the test container water bath, completely submerging the protruding 2mm-mesh net. The 72-hour-H_2O saturated PCNL-derived fragment was then placed directly within the center of the 2mm-mesh net using forceps and images by phone were immediately obtained of T-0 (Fig. 7 and 8A, D).

ESWL-DERIVED PARTICLE EXPERIMENTAL DESIGN

In this experiment, the ESWL instrument was set to a shock rate of 90 shocks/min, coupling pressure of 4, power level of 3, with increments of 100 shocks per treatment. After each 100-shock ESWL treatment, the ESWL-derived particles sieved within the 2mm-mesh net and the ESWL-derived particles small enough to pass through the 2mm-mesh net and into the water bath were imaged by phone, then separately collected and processed.

ESWL-derived particles sieved within the 2mm-mesh net

After each 100-shock ESWL treatment, the ESWL-derived particles sieved within the 2mm-mesh net were collected using forceps, tapped onto a Kim wipe, placed into a weigh boat, imaged by phone, and weighed. ESWL-derived particles that fell through during this collection were obtained at the bottom of the calibration container with forceps or a pipette. Subsequently, an additional 1000mL of 18.2 MilliQ water was poured into the calibration container water bath and the ESWL-derived particles were carefully placed back into the 2mm-mesh net for another

treatment cycle. At this point, if any small ESWL-derived particles fell through, they may have been left at the bottom of the container. Although, an electric pipette and forceps were utilized to capture larger ESWL-derived particles and transfer them back into the center 2mm-mesh net prior to initiating the next 100-shock treatment. A final representative image of the remaining ESWL-derived particles within the 2mm-mesh net was obtained by phone. The process was repeated until no ESWL-derived particles were detected in the center 2mm-mesh net. For analysis, the weights obtained after each 100-shock ESWL treatment were processed to generate representative graphical outputs using Microsoft Excel (Fig. 17A, Table 3).

ESWL-derived particles collected from the ESWL calibration container water bath

After each 100-shock ESWL treatment, the calibration container water bath was drained in 120mL increments using the Med Lab Supply hand vacuum pump with pressure gauge (https://www.medical-and-lab-supplies.com/hand-vacuum-pump-with-pressure-gauge.html) into a 1000mL beaker. An Accu-Jet Pro electronic pipette controller (https://www.brandtech.com/product/accu-jet-pro/) attached to a 10mL tip, with 1cm of the tip cutoff, was used to collect visible, broken fragments within the test container. The beaker with the water bath containing the ESWL-derived particles was left for 10 minutes at an angle, allowing for the ESWL-derived particles to settle. Subsequently, the 1000mL solution was filtered through a 500mL vacuum filtration system using GE Healthcare Life Sciences Whatman 0.47µm mixed cellulose ester membrane filter paper. The filter paper was then transferred into a labeled petri dish for imaging and quantification. This procedure was repeated with each 100-shock ESWL treatment.

REFLECTIVE LIGHT IMAGING AND ESWL-DERIVED PARTICLE GRAIN SIZE QUANTIFICATION AND CLASSIFICATION

Loose ESWL-derived particles from the water bath collected from each 100-shock ESWL treatment were placed within an orange rubber ring on a weigh boat to be imaged, quantified, and characterized by grain size. Complete 4 x 4 stitched tiled images (each comprising 14443 x 9626 pixels; 63.96mm x 42.64mm) were obtained using reflective light microscopy on the Zeiss Axio Zoom.V16 microscope with a total magnification of 7x. Subsequently, all loose ESWL-derived particles from each 100-shock ESWL treatment were carefully transferred into individually labelled Eppendorf tubes for storage. The images were then uploaded into Adobe Photoshop and each loose ESWL-derived particle was carefully outlined by hand and filled with one selected color (RGB of 210 for red, 0 for green, and 255 for blue) to ensure more accurate selection during grain size quantification (Fig. 8B, E). Each image had a scale of 4.429μm/px. Each individual image was uploaded into the Zeiss AxioVision program to be processed using a brightness of -0.56, contrast of 1.12, gamma of 1.00, sigma of 32, shading correction brightness of -185, edge enhancement delineate threshold of 25, edge enhancement delineate size of 3, deletion of artifact minimum of 0 and maximum of 90753696 with selected fill holes, and automatic object separation mode of watershed and settings tolerance of 2. The RGB selection range for the loose ESWL-derived particles from PCNL-derived fragment 106F2 were 204-223 for red, 0-104 for green, and 192-255 for blue. The RGB selection range for the loose ESWL-derived particles from PCNL-derived fragment 106F4 fragments were 207-223 for red, 0-104 for green, and 216-255 for blue. Using these settings, a final output containing the total number of stones and each measured (largest) diameter was obtained and converted into an XML and XLSX file. Subsequently, this data was characterized and visually graphed using Microsoft Excel according to the Wentworth

grain size scale (Wentworth, 1922). Size frequency distributions could only be determined from loose ESWL-derived particles because thin sections made from epoxied ESWL-derived particles can significantly under sample the grain sizes due to the polishing-impact on the elevation of the plane of section.

EPOXY-PLUG EMBEDDING OF LOOSE ESWL-DERIVED PARTICLE SUBSET

Loose ESWL-derived particles collected from the first 100-shock ESWL treatment for both PCNL-derived fragments 106F2 (106F2-S1) and 106F4 (106F4-S1) contained the largest number of particles, thus, were selected for epoxy embedding. The loose ESWL-derived particle groups, 106F2-S1 and 106F4-S1, were carefully placed onto a Buehler MET Grip Liner Adhesive within a 1in x 1in Buehler SamplKup. Properly mixed Buehler EpoThin 2 media (22.6g hardener and 50.0g resin) without air bubbles was poured onto the adhesive liner within the SamplKup, then placed into the Buehler SimpliVac machine for infiltration at 1 cycle for 30 seconds at -25.7inHg. The samples were then placed in a heater overnight to cure. The following day, the adhesive liner was slowly removed, and the hardened epoxy-embedded plugs were dislodged from the SamplKup. The epoxy-embedded ESWL-derived particle samples of 106F2-S1 and 106F4-S1 were polished on the fragment-exposed surface using the Buehler AutoMet 250 Polisher in the following sequence: (1) Buehler 800 Grit (5μm) or 600 Grit to grind into the stone and remove epoxy; (2) Buehler 3μm diamond paste on a Buehler Trident Pad; and (3) Buehler Alumina paste on a Buehler MicroCloth. The epoxy plugs were then submerged in a beaker of ethanol and placed in the Buehler UltraMet 2003 Sonic Cleaner containing Simple Green All Purpose Cleaner diluted with water. This procedure was completed by L. Todorov (author) at Buehler in Lake Bluff, IL. The epoxy-embedded 106F2-S1 and 106F4-S1 samples were imaged on the Zeiss Axio

Zoom.V16, Axio Observer.Z1, and Zeiss LSM 880 microscopes before being sent to Wagner Petrographic Ltd. in Linden, Utah to be converted into standard-sized (24mm x 46mm), uncovered (no slip), doubly polished thin sections with a thickness of ~25μm.

PREPARATION OF THIN SECTIONS 106F3-1 AND 106F3-2

PCNL-derived kidney stone 106F3 was selected to be thin sectioned. A 1in x 1in Buehler SamplKup was assembled using the Buehler Release Agent and filled with properly mixed EpoThin 2 media. When the epoxy hardened, the PCNL-derived fragment 106F3 was strategically oriented with mounting clay using the micro-CT data from the North Star Imaging X3000 Industrial 3D X-Ray Inspection system onto the hardened epoxy, selecting a line of section (cut) with the optimal orientation for the visualization of the crystal growth axis within the complete thin section. Additional epoxy was carefully added using a syringe until the selected line of section was reached and the epoxy on the partially submerged PCNL-derived fragment 106F3 was allowed to cure overnight. The following day, the sample was removed from the SamplKup and the dried-epoxy meniscus was grinded off using sandpaper. The epoxy-embedded PCNL-derived fragment 106F3 was cut at the selected orientation (epoxy surface) using the Buehler IsoMet Low Speed Precision Cutter with the Buehler IsoMet 10LC Precision Blade and 1.75in aluminum flange set. The non-epoxy embedded PCNL-derived fragment 106F3 portion that detached from the embedded plug was collected and stored for further decalcification experiments. The epoxy-embedded plug was then returned to the SamplKup, placed in the SimpliVac system with loaded EpoThin 2 epoxy, completely submerged with epoxy while the system was run for 10 cycles at 1 minute with -25.4inHg, and left to cure overnight to allow epoxy to infiltrate the stone through the pore space.

The following day, the epoxy-embedded plug containing the PCNL-derived fragment 106F3 was removed from the SamplKup and prepared for polishing by placing it within the Buehler central force specimen plate (5.1in and 6.1in) with two blank epoxy plugs, using the Buehler Specimen Loading Fixture. The epoxy-embedded plug containing PCNL-derived fragment 106F3 was polished on the surface closest to the stone using the Buehler AutoMet 250 Polisher in the following sequence: (1) Buehler Diamond Grinding Red (75µm) Magnetic Disk; (2) Buehler Diamond Grinding Yellow (35µm) Magnetic Disk; (3) Buehler PSA Backed MicroCut 800 [P1500] (13µm) disk; (4) Buehler MetaDi Diamond Green Paste (3µm) on a Buehler Trident Polishing Cloth with MetaDi Fluid; and (5) Buehler Alumina paste on a Buehler MicroCloth. The sample was then submerged in a beaker of ethanol and placed in the Buehler UltraMet 2003 Sonic Cleaner containing Simple Green All Purpose Cleaner diluted with water. A standard sized (24mm x 46mm) microscope slide was placed on a rectangular piece of MetGrip Liner Adhesive and properly mixed EpoThin 2 media was evenly coated in the center using a mixing stick. The 106F3 epoxy-embedded plug was placed on the slide and left to cure overnight using the Buehler PetroBond on a hot plate at 35-40°C.

A thin section containing the PCNL-derived fragment 106F3 epoxy-embedded plug was cut ~500 µm from the glass slide using the Buehler IsoMet High Speed Pro using the IsoMet 15HC Blade and the 1.38in (35mm) aluminum flange set at settings 5 mm/min, cutting depth of 40mm, 4000 RPM, serial cut off and smart cut off selected, coolant set to off, blade dress set to off, and manual dress option set to off. The thin section was named 106F3-1, while the remaining epoxy-embedded sample was named 106F3-2. The 106F3-1 thin section was then placed into the Buehler Stage Micrometer using Buehler Lapping Oil and polished to ~60µm thickness using the AutoMet 250 Polisher in the following sequence: (1) Buehler Purple Diamond Grinding (55µm) Disk; (2)

Buehler Terra Diamond Grinding (9μm) Disk; (3) Buehler MetaDi Diamond Green Paste (3μm) on a Buehler Trident Polishing Cloth with MetaDi Fluid; and (4) Buehler Alumina paste on a Buehler MicroCloth. Some regions of the 106F3-1 were plucked during thin section polishing and preparation. This procedure was completed by L. Todorov (author) at Buehler in Lake Bluff, IL. The 106F3-1 thin section was imaged on the Zeiss Axio Zoom.V16, AxioScan.Z1, Axio Observer.Z1, and Zeiss LSM 880 microscopes before being sent to Wagner Petrographic for final polishing to ~25μm thickness. The 106F3-2 embedded sample was imaged on the Zeiss Axio Zoom.V16 before also being sent to Wagner Petrographic to be converted into standard-sized (24mm x 46mm), uncovered (no slip), doubly polished thin sections with a thickness of ~25μm. The received thin sections were then imaged on the Zeiss AxioScan.Z1 and LSM 980 Confocal microscopes.

BRIGHTFIELD (BF), POLARIZATION (POL), PHASE CONTRACT (PC), AND RING APERATURE CONTRAST (RAC) MICROSCOPY

A wide variety of optical modalities were applied in the present study to image the kidney stone thin sections (Sivaguru et al., 2012, 2014a, 2014b, 2016, 2018, 2021; Kolossov et al., 2017; Singh et al., 2017; Urban et al., 2016; Huff et al., 2015). These include BF, POL, PC, and RAC as described before (Sivaguru et al., 2012, 2016, 2018). We have used a suite of Zeiss instruments with the appropriate optical magnifications to render an ultimate spatial resolution of 250nm. These include: (1) Zeiss Axio Zoom.V16 microscope with a DL 450 LED light source base, Axiocam 512 color camera, and a 1.0x Plan-NeoFluar Z NA 0.25 objective for both reflective and transmitted light microscopy (BF and POL); Zeiss AxioScan.Z1 whole slide scanner system with a TL LED lamp, Hitachi HV-F202SCL camera, and a Plan Aprochromat 10x/ 0.45 NA objective

(for BF, POL, and RAC); and (3) Zeiss Axio Observer.Z1 microscope with TL Halogen lamp, Zeiss Axiocam 506, Analyzer DIC Transmitted Light Reflector with polarizer set to 0° (for POL), Plan Aprochromat 10x/0.45 NA Ph1 M27 objective, Plan Aprochromat 20x/0.80 NA Ph2 DICII objective, and Plan Aprochromat 63x/1.40 Oil Ph3 objective (for BF, POL, and PC). All microscopy in this study was completed in the Microscopy and Imaging Core Facility of the IGB on the Illinois campus. This was the first North American laboratory selected as the Zeiss Labs@Location Partner by Carl Zeiss LLC, a recognition that facilitated the integrated assemblage of all the microscopy modalities applied in this study.

CONFOCAL AUTO-FLUORESCENCE (CAF) AND AIRYSCAN SUPER-RESOLUTION AUTOFLUORESCENCE (SRAF)

The fracture patterns were characterized, and specific locations were selected to be further investigated using the Zeiss LSM 880 and LSM 980 Scanning microscopes with Airyscan Super-Resolution (Huff, 2015). These instruments have a resolution significantly greater than all other currently available confocal diffraction-limited microscopy techniques by a factor of 1.7, to provide a spatial resolution of ~140nm (Sivaguru et al., 2014; Kolossov et al., 2017; Urban et al., 2016; Huff, 2015). We have used these systems in both super-resolution autofluorescence (SRAF; scan zoom ≥ 2; Figs 6A,D, E, 14H, 16B) and confocal auto fluorescence (CAF; scan zoom < 2; Figs. 6B, C, F, G, H, 12, 14A-G, 16A, C) modes. Excitation and emission wavelengths that were collected on the LSM 880 include: 405nm excitation (emission collected at 450nm; blue), 488nm excitation (emission collected at 525nm; green), and 561nm excitation (emission collected at 593nm; red). Excitation and emission wavelengths that were collected on the LSM 980 include: 353nm excitation (emission collected at 465nm; blue), 492nm excitation (emission collected at

517nm; green), and 577nm excitation (emission collected at 603nm; red). On the LSM 880, an internal photo-multiplier tube detector was used to scan selected locations using a Plan-Aprochromat 63x/1.4 NA Oil immersion DIC M27 objective. On the LSM 980, the objectives used were the Plan Aprochromat 10x/0.45 NA M27 and Plan Aprochromat 20x/0.8 NA M27. Simultaneously, transmitted-light images were obtained using a 561nm laser transmission photomultiplier (T-PMT) detector on the same system (Figs. 3B, 4A, C, E, G; Sup Figs. 6, 7, and 8). The main beam splitters (MBS used in the light path of the detector were MBS 488/561 for visible and MBS 405 for invisible light paths for SRAF, CAF, and T-PMT. SRAF and CAF also the dichronic beam splitter SPS SP 615. Raw data images from 32 Airyscan detectors were processed using the Airyscan processing modality using the auto-2D to obtain a super-resolution image.

IMAGE ADJUSTMENTS, ANALYSIS, PREPARATION, AND PRESENTATION

All images were processed using the Zeiss Zen Blue and/or Black software to display either minimum and maximum or best-fit properties (Cromey, 2010) unless otherwise stated in the figure legends. In addition, red-green-blue (RGB) curves were adjusted individually or together to highlight all the crystal intensities in individual frames across the whole specimen. Where required, a non-linear gamma correction of 0.45 or 0.70 was applied to enhance faint AF crystal intensities in the same Zen program under the spline display mode property and all other corrections are presenting in the corresponding figure legends. All raw data was stored in native CZI and then exported as TIF files with no compression after adjusting the display properties. Final images were cropped, resized, adjusted for optimal brightness and contrast, and assembled using Adobe Photoshop (Adobe Systems Inc., San Jose, CA) to fit the required format.

RAMAN SPECTROSCOPY OF THIN SECTION 106F3-1

A WITec Alpha 300RA AFM-Raman system was used to investigate the composition of thin section 106F3-1. The UHTS 600 VIS spectrometer associated with the AFM-Raman system was used for better sensitivity and peak separation. Two large contextual areas using high magnification 20-100x objectives were scanned and imaged. The large image scans were stitched automatically using the corresponding software. To prevent autofluorescence, a 532nm laser was used with 0.1s integration time and 150-250 points per line setting. Raman images were converted to pseudo-color-coded images and overlaid correlatively on transmitted light BF images for easy comparison. Raman spectra were background subtracted prior to final analysis using the Project 5 WITec software. The acquired Raman peaks were correlated and compared with previously published Raman peaks for human kidney stones (Takasaki, 1996; Balan et al., 2019; Castiglione et al., 2019; Sivaguru et al., 2021; Saw et al., 2021).

APPENDIX B
SUPPLMENTARY REFERENCES

Balan, V., Mihai, C.-T., Cojocaru, F.-D., Uritu, C.-M., Dodi, G., Botezat, D., & Gardikiotis, I. (2019). Vibrational Spectroscopy Fingerprinting in Medicine: from Molecular to Clinical Practice. *Materials*, *12*(18), 2884. https://doi.org/10.3390/ma12182884

Castiglione, V., Sacré, P.-Y., Cavalier, E., Hubert, P., Gadisseur, R., & Ziemons, E. (2018). Raman chemical imaging, a new tool in kidney stone structure analysis: Case-study and comparison to Fourier Transform Infrared spectroscopy. *PLoS ONE*, *13*(8), e0201460. https://doi.org/10.1371/journal.pone.0201460

Cromey, D. W. (2010). Avoiding Twisted Pixels: Ethical Guidelines for the Appropriate Use and Manipulation of Scientific Digital Images. *Science and Engineering Ethics*, *16*(4), 639-667. https://doi.org/10.1007/s11948-010-9201-y

Huff, J. (2015). The Airyscan detector from ZEISS: confocal imaging with improved signal-to-noise ratio and super-resolution. *Nature Methods*, *12*(12), i-ii. https://doi.org/10.1038/nmeth.f.388

Kolossov, V. L., Sivaguru, M., Huff, J., Luby, K., Kanakaraju, K., & Gaskins, H. R. (2018). Airyscan super-resolution microscopy of mitochondrial morphology and dynamics in living tumor cells. *Microscopy Research and Technique*, *81*(2), 115-128. https://doi.org/10.1002/jemt.22968

Patil, A. V. (2010). A Novel 5-Part Percutaneous Access Needle With Glidewire Technique (5-PANG) for Percutaneous Nephrolithotomy: Our Initial Experience. *Urology*, *75*(5), 1206-1208. https://doi.org/10.1016/j.urology.2009.11.027

Singh, R., Sivaguru, M., Fried, G. A., Fouke, B. W., Sanford, R. A., Carrera, M., & Werth, C. J. (2017). Real rock-microfluidic flow cell: A test bed for real-time in situ analysis of flow, transport, and reaction in a subsurface reactive transport environment. *Journal of Contaminant Hydrology*, *204*, 28-39. https://doi.org/10.1016/j.jconhyd.2017.08.001

Sivaguru, M., Eichorst, J. P., Durgam, S., Fried, G. A., Stewart, A. A., & Stewart, M. C. (2014a). Imaging horse tendons using multimodal 2-photon microscopy. *Methods*, *66*(2), 256-267. https://doi.org/10.1016/j.ymeth.2013.07.016

Sivaguru, M., Fried, G. A., Miller, C. A. H., & Fouke, B. W. (2014b). Multimodal Optical Microscopy Methods Reveal Polyp Tissue Morphology and Structure in Caribbean Reef Building Corals. *Journal of Visualized Experiments*(91). https://doi.org/10.3791/51824

Sivaguru, M., Mander, L., Fried, G., & Punyasena, S. W. (2012). Capturing the Surface Texture and Shape of Pollen: A Comparison of Microscopy Techniques. *PLoS ONE*, *7*(6), e39129. https://doi.org/10.1371/journal.pone.0039129

Sivaguru, M., Urban, M. A., Fried, G., Wesseln, C. J., Mander, L., & Punyasena, S. W. (2016). Comparative performance of airyscan and structured illumination superresolution microscopy in the study of the surface texture and 3D shape of pollen. *Microscopy Research and Technique*, *81*(2), 101-114. https://doi.org/10.1002/jemt.22732

Takasaki, E. (1996). Carbonate in Struvite Stone Detected in Raman Spectra Compared with Infrared Spectra and X-Ray Diffraction. *International Journal of Urology*, *3*(1), 27-30. https://doi.org/10.1111/j.1442-2042.1996.tb00625.x

Urban, M. A., Barclay, R. S., Sivaguru, M., & Punyasena, S. W. (2016). Cuticle and subsurface ornamentation of intact plant leaf epidermis under confocal and superresolution microscopy. *Microscopy Research and Technique*, *81*(2), 129-140. https://doi.org/10.1002/jemt.22667